Carl von Ossietzky Universität Oldenburg

Master Thesis
in Engineering Physics

Planing, Simulation and Preparation of a Magnetic Resonant Imaging Experiment based on the Detection of Anisotropic gamma-Radiation from Hyperpolarized Isomers

Submitted by

Robin Engel

Carl-von-Ossietzky Universität Oldenburg
European Center for Nuclear Research
Hochschule Emden/Leer

Supervisors

Prof. Dr. Walter Neu
Hochschule Emden/Leer
Carl-von-Ossietzky Universität Oldenburg

Dr. Magdalena Kowalska
European Center for Nuclear Research

Geneva, July 2018

Acknowledgements

To the collaboration

An extraordinary thanks goes to Prof. Dr. Jean-Noël Hyacinthe and his team, without whom this project would not be possible. Many thanks for all the fruitful discussions, so much knowledge on hyper-polarized MRI, a lot of time and effort and last but not least providing your laboratory and equipment for the measurements.

A big thanks also goes to Luis Fraile and Jose Manuel Udias Moinelo from the University of Madrid, and to Victor Sanchez-Tembleque Verbo and Miguel Garcia from their group, who have developed and built the suitable detectors. And last but not least, to Renaud Blaise Jolivet, who was with this project continuously from the beginning, supporting it with his expertise on the medical side of the project as well as with organizational work and material support.

To my team

Here, my very first thanks goes to my supervisor Dr. Magdalena Kowalska, who initiated this project in the first place and with never-ending energy organized the expertise, people and devices needed to get so far in so little time.

Second, I want to thank Prof. Dr. Walter Neu, who with continuous advice and support long before the work on this thesis began, has given me first the perspective and later the chance to work on a thesis in such a great environment like CERN and ISOLDE in the first place.

Further thanks goes to Stavroula Pallada, who helped with her experiences in medical physics as well as many of the little every-day problems of the project. Alexandre Dorsival helped me find a way to safely handle radioactive iodine, Francois Garnier was pleasant and reliable in milling the parts for the decy setup, Thierry Stora helped with advice on the collection of radioactive isotopes and Richard Catherall had an open and forgiving ear for the scheduling of space in the fume-hood. Many more have helped in this project and even more have simply made this a very special place to work at, so I will finish with a big thanks to the whole group at and around ISOLDE!

CARL-VON-OSSIETZKY UNIVERSITÄT OLDENBURG
HOCHSCHULE EMDEN / LEER
EUROPEAN CENTER FOR NUCLEAR RESEARCH

Abstract

Planing, Simulation and Preparation of a Magnetic Resonant Imaging Experiment based on the Detection of Anisotropic gamma-Radiation from Hyperpolarized Isomers

by Robin Engel

In 2016, the proof of principle for a new method of imaging was presented [1], which uses many elements of traditional Magnetic Resonant Imaging, but replaces the detection of RF induction signals with that of the anisotropic gamma-emission from a hyper-polarized radioactive noble gas. Since gamma-radiation is in comparison very easy to detect, this method is sensitive to concentrations of imaged nuclei that are up to ten orders of magnitudes lower than those needed in conventional MRI. Therefore, it has the perspective of combining the advantages of nuclear tracers, as they are used in SPECT and PET, with the higher spatial resolution of MRI. In addition to presenting a software for numerical simulations of the spin precession and nuclear emission behavior during magnetic resonance experiments on hyper-polarized radioactive xenon, this thesis documents the development of two dedicated setups. The first is dedicated to extracting ^{131m}Xe, the radioactive tracer required for the measurements, from commercially available ^{131}I. The second setup is designed for magnetic resonance experiments on hyper-polarized xenon, capable of using both the anisotropic gamma emission from radioactive nuclei as well as induction signals from stable isotopes for detection. It utilizes an existing low-field MRI-scanner and Si-PMT based gamma detectors in combination with elements from a spin-exchange optical pumping setup developed for hyper-polarized MRI on stable Xenon. Both setups were planned, built and tested in the frame of this thesis and are ready for commissioning.

List of Figures

List of Tables

Abbreviations

APD	Avalanche Photo Diode
CERN	Conseil Européen pour la Recherche Nucléaire
CMZ	Cates-Miller-Zheng
CT	Computer Tomography
DAQ	Data AcQuisition system
DNP	Dynamic Nuclear Polarization
GUI	Graphical User Interface
FID	Free Induction Decay
HESGE	Haute Ecole Spécialisée GEnéve
HP	Hyper-Polarized
ISOLDE	Isotope Separator On Line DEvice
MRI	Magnetic Resonance Imaging
NMR	Nuclear Magnetic Resonance
PET	Positron Emission Tomography
PNI	Polarized Nuclear Imaging
RF	Radio Frequency
SEOP	Spin Exchange Optical Pumping
SiPM	Silicium Photo Multiplier
SPECT	Single Poton Emission Tomography

Physical Constants

Speed of light	c	=	$2.997\ 924\ 58 \times 10^{8}\ m/s$
Electron charge	e	=	$-1.602\ 176\ 56 \times 10^{-19}\ As$
Electron mass	m_e	=	$9.109\ 382\ 91 \times 10^{-31}\ Kg$
Nuclear magneton	μ_N	=	$5.05 \times 10^{-27}\ J/T$
Boltzmann constant	k	=	$1.38064852 \times 10^{-23}\ m^2kg/s^2K$
Planks constant	h	=	$1.0545718 \times 10^{-34}\ Js$
Planks constant (reduced)	$\hbar$	=	$h/(2\pi)$

Symbols

a_m	Population probabilities/densities of the nuclear m-states
m	Index of nuclear m-state or Zeeman level
m_j	Angular momentum along the magnetic field
$\mathbf{r}_\gamma$	Vector representing a `ray` from sample element to detector element
$\mathbf{r}_d$	Vector pointing to the location of a detector element
$\mathbf{r}_s$	Vector pointing to the location of a sample element
t	Time
t_{del}	Delay time between two RF pulses
t_{pol}	Duration of optical pumping

A	Complex matrix proportional to the Fourier transform of ρ
A_λ	Angular distribution coefficients, specific to the decay type and mother nucleus
B	Magnetic field
B_0	Constant magnetic field in an MR experiment
B_1	Rotating component of the magnetic field of a RF-wave in a sample
B_λ	Nuclear Orientation parameters
E_m	Energy of nuclear m-states
F_λ	F-coefficients, same as A_λ but only for one multipolarity
$\mathbf{G}$	A magnetic field gradient
G_λ	Perturbation parameters accounting for relaxation effects
I	Spin
$\mathbf{M}$	Magnetization vector
P	Polarization
R	A detector count-rate
S_R	Real spin moment of the sample
S_I	Imaginary spin moment of the sample
T	Temperatur
T_1	Longitudinal relaxation constant
T_2	True transversal relaxation constant
T_2^*	Measured transversal relaxation constant
$T_{1/2}$	Half-life of a state
U_λ	Deorientation coefficients due to a decay between polarization and measurement
W	Directional distribution of gamma-radiation
γ	Gyromagnetic ratio
γ_{op}	Rate of optical pumping on rubidium
γ_{SE}	Spin exchange rate
γ_{trap}	Depolarization rate through radiation trapping
θ_{pulse}	Azimuthal angle an RF-pulse turns the magnetization M by
θ	Angle between emission and magnetization $\mathbf{M}$
θ_f	Polar angle between magnetization $\mathbf{M}$ an $z - axis$
θ_{eff}	Effective angle between ray vector and magnetization $\mathbf{M}$

κ_{sd}	Spin destruction rate through collissions
λ	Summation index
μ	Nuclear magnetic moment
ρ	Density distribution of radioactive xenon
τ	Time for which gradient fields are active
τ_{pulse}	Duration of an RF-pulse
ϕ	Azimuthal angle between magnetization and x-axis
ω_L	Larmor frequency
Γ	Self-relaxation rate ($\Gamma = 1/T_1$)

Contents

Chapter 1

Introduction

Since the discovery of X-ray radiation by Conrad Röntgen in 1895, a variety of methods has been developed that enables us to take pictures of the insides of solids that are not transparent in the visible spectrum. All use one or another type of radiation that can penetrate the pictured object, be it X-rays (simple X-ray images and computer tomography (CT)), gamma-rays from nuclear decay (single photon emission computer tomography (SPECT) and positron emission tomography (PET)), ultrasound (ultrasound imaging) or radio-waves (magnetic resonant imaging (MRI)). All of these methods are widely used, especially in medical applications, and all have their unique advantages and limitations, but new developments constantly push the limits of these techniques.

Relating to the respective physical phenomena that they are based on, each method has some principle limitations that are difficult to compensate despite increasingly high degrees of sophistication. For example, the spatial resolution of PET is limited by the mean path that an emitted positron travels before decaying into two gamma-rays, whereas in MRI, this limit is given by the strength of the applied magnetic fields and field gradients, which typically allows for a finer resolution. On the other hand, PET allows imaging with chemically selective tracers that bind to specific kinds of tissue in the body, to a degree that contrast agents in MRI struggle to compete with.

Therefore, the recent years have seen a rising interest in incorporate some of these methods into one measurement setup, so as to achieve an imaging technique that

combines both advantages [5]. Many of these designs take pictures with two of these modalities independently and digitally overlay the two images afterwards.

Beyond that, Zheng et. al. [1] have in 2016 presented the proof of principle for a new modality, calling it polarized nuclear imaging (PNI). Here, the spatial resolution is achieved using magnetic field gradients like in MRI, but instead of picking up the spatial information by detecting low-energetic RF photons, this method uses gamma-rays from nuclear tracers as it is done in SPECT and PET. This is an exciting discovery, since the approach offers the potential to combine the advantages of the respective methods in one single modality.

At the same time, as will be discussed in more detail in chapter 3, this approach also combines the technical challenges of several fields. That makes it an especially interesting method to study and develop. One of the relevant fields involves the directivity of radioactive decay (in this case gamma-photons) from polarized nuclei, which is closely related to other experiments that our research group at CERNs radioactive ion beam facility ISOLDE performs [6]. Further, the ISOLDE facility is capable of producing most if not all of the radioactive tracer nuclei that PNI could potentially work with.

This background gave rise to the work presented in this thesis, with goal to explore the principles of this new imaging modality and to prepare for experiments that reproduce and expand on the findings presented by Zheng et al. in late 2016.

In order to gather the necessary expertise of the various involved fields, we have formed a collaboration with the groups of Jean-Noël Hyacinte at the HESGE in Geneva, who specializes in hyperpolarized MRI on stable xenon, as well as the group of Luis Fraile and Jose Manuel Udias Moinelo at the University of Madrid, whose research is in the area of specialized gamma-detectors.

Chapter 2

Theoretical Background

This chapter gives some theoretical background necessary to follow the topics presented here. Since it touches on several topics that have seen a large amount of research in the past, the discussion will be somewhat limited in depth in favour of brevity.

2.1 Nuclear Orientation

Any nucleus with non-zero spin exhibits a magnetic dipole moment, and those with a spin $> 1/2$ additionally an electric quadrupole moment, which interact with local magnetic fields and electric field gradients respectively. These fields can be produced in the laboratory, but unpaired electrons within the atomic shell and the chemical environment of the atom often generate very strong fields that interact with the nucleus [2]. Such interactions split a nuclear energy level with the spin I into $2I+1$ sublevels with quantum numbers $m = I, I-1, ..., -I$. If we ignore the influence of quadrupolar moments (their influence on the following descriptions is mostly negligible), these equidistant energy states can be described with $E_m = -\gamma B_0 m\hbar$ and will be referred to as the *nuclear m-states* in this work. Here, γ is the gyromagnetic ratio and B_0 is the magnetic field. In thermal equilibrium, these states have population probabilities a_m given by the Boltzmann distribution.

$$a_m = \frac{e^{-E_m/kT}}{\sum_m e^{-E_m/kT)}} \tag{2.1}$$

As a way to picture this energy splitting of states, we can think of each state as a certain allowed angle between a vectorial representation of the nuclear dipole moment and the magnetic field. To minimize its energy, any magnetic dipole tends to align with a magnetic field, so that each possible angle between both represents a different energy of the corresponding m-state. Since E_m is a function of the magnetic field, it is apparent from equation 2.1 that the m-states of lower energy will have a slightly higher population probability. Such a deviation in the m-state distribution from uniformity corresponds to a macroscopic alignment of the overall orientation in the nuclear spins and is therefore described as *nuclear orientation* or *magnetization*. Experimentally, a direct measurement of the m-state populations is usually not possible[1]. However, any distribution function can be expressed in terms of its statistical moments. For oriented nuclei, the statistical moments are linked to the respective degree of multipolarity in the nuclear state. Most experimental works use the parameter of polarization, which is defined as the first statistical moment of a_m over m.

$$\sum_m (m/I)a_m = P(I) = f_1(I) = -\sqrt{(I+1)/3I}B_{\lambda=1}(I) \tag{2.2}$$

The higher statistical moments are important for respectively higher multipolarity radiation, but the only other commonly used term is the *alignment* or $f_2(I)$:

$$f_2(I) = \sum_m (m/I)^2 a_m - \frac{1}{3}(I+1)/I \tag{2.3}$$

$$= -\sqrt{(2I+3)(I+1)(2I-1)/45I^3}B_{\lambda=2}(I) \tag{2.4}$$

This definition of f_1 and f_2 was already introduced by *Tolhoek and Cox 1953* [7]. Other works (see [2] for a summary) have used a variety of parameters like the *polarization* $P(I)$ or *statistical tensors* ρ^q_λ. These conventions are mostly equivalent except for the normalization. In this work, we will use the *nuclear orientation parametes* B_λ introduced by *Blin-Stoyle and Grace 1957* [8].

[1] Except in a spin 1/2 system, where the distribution can be fully reconstructed from a measurement of the magnetization.

2.1.1 Radiation from Oriented Nuclei

The orientation of a nucleus, i.e. the distribution of its m-state populations, affects the direction into which it emits radiation, since we can model this radiation with a quantum-physical description of multipole radiation. Such a derivation was performed by [7, 8] and can also be found the pertinent literature[2]. For this thesis it shall be sufficient to quote the result that the directional distribution of gamma-radiation $W(\theta)$ is only dependent on even orders of the multipolarity λ and can be described as:

$$W(\theta) = 1 + \sum_{\lambda even} B_\lambda U_\lambda G_\lambda A_\lambda P_\lambda(\cos(\theta)) \tag{2.5}$$

One may understand this equation as illustrated in figure 2.1: The direction of the eventual gamma-emission is dependent on the nuclear orientation of the final state, described by B_λ multiplied with U_λ and G_λ. Radiation from some nuclear transitions exhibit stronger asymmetric radiation than others, which is described by the *angular distribution coefficients* A_λ.

The initial oriented state $|I_o\rangle$ is described in terms of the previously introduced orientation parameters B_λ. Between this state and the initial state $|I_i\rangle$ from which a radiation will be observed, a varying time may elapse, during which the nuclear orientation may change. One possibility is an intermediate decay of the nucleus. The effect of such an intermediate decay depends again on the multipolarity of the emitted radiation and is described by the *deorientation coefficients* U_λ. In the absence of intermediate decays the nuclear orientation will still *relax* with time due to interactions of the nuclear dipole and quadrupole moments with the electromagnetic fields of the environment. This effect can be modeled with the *perturbation coeffiecients* G_λ. However, since this describes the same effects that we model as *relaxation* in magnetic resonance terms, we chose to use the later model and neglect the perturbation coefficients (by setting their value to unity) in this equation.

After modeling the nuclear orientation up to observed state $|I_i\rangle$, the angular distribution is only dependent on the *angular distribution coefficients* A_λ, which are specific to the applicable transition of nuclear levels. Again, they depend on the difference in spin I and the possible change of parity between observed and final state $|I_i\rangle$ and $|I_f\rangle$. Some experiments observe correlations between two successive radiations, which allows inferences about the intermediate state $|I_m\rangle$. P_λ represents

the Legendre polynomial of order λ and θ is the azimuthal angle between radiation and z-axis around which the radiation is axially symmetric. A more detailed and quantitative description of this formalism may be found in [2], Chapter 2: *Nuclear Orientation Formalism* by K.S. Krane.

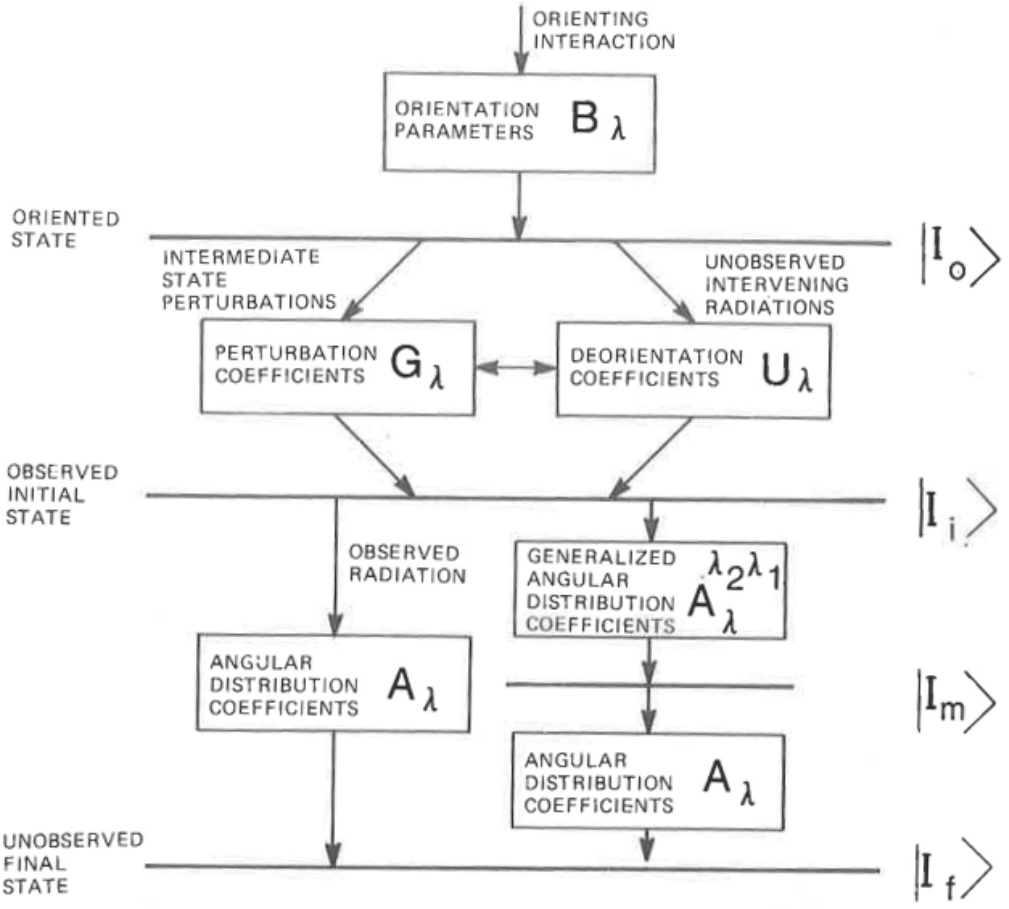

FIGURE 2.1: Illustration of the different parameters necessary for describing radiation from oriented nuclei. Adapted from [2], Chapter 2: *Nuclear Orientation Formalism* by K.S. Krane.

The resulting angular distribution is plotted in two and three dimensions in figure 2.2 for large polarizations.

2.2 Magnetic Resonance Techniques

We call the method presented in this thesis gamma-MRI, because it functions in many ways just like regular Magnetic Resonance Imaging, although replacing some

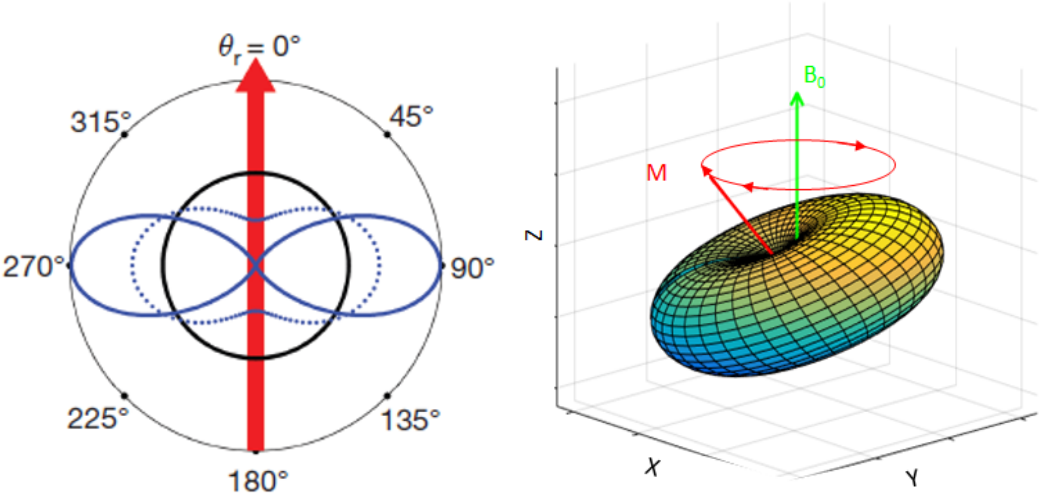

(A) Expected gamma-anisotropy at 0%, 70% and 100% (black, dotted and blue line respectively) polarization. Adapted from [1].

(B) A three-dimensional plot of the expected gamma anisotropy of a nuclues that precesses around the magnetic field axis B_0 after an RF pulse, as will be described in section 2.2.1.1.

FIGURE 2.2: Plots of angular distribution of gamma decay in two and three dimensions. The plotted radius corresponds to the emission probability in that direction. The red arrow represents the magnetization vector.

elements in order to increase the sensitivity. To understand gamma-MRI, it is therefore necessary to first comprehend the principles of regular MRI. In turn, one cannot explain Magnetic Resonance Imaging without describing Nuclear Magnetic Resonance (NMR), on which the former modality is based.

I will therefore open with a mostly qualitative description of NMR and MRI. A more detailed quantitative description may be found in [3, 9] or other pertinent literature. There are a few main components in any MR setup, which shall be listed here to define the terminology used in this thesis:

- **The external field B_0:** This is a constant magnetic field in which the sample is located. Following a common convention, B_0 shall always point along the coordinate systems $z - axis$ in this work.
- **RF-coil:** The RF-coil provides a radio-frequency electromagnetic wave within the sample. It is oriented so that the direction of its magnetic field component is always transversal to B_0. This undulating magnetic field is referred to as

B_1[2]. In addition to providing the B_1 field, the RF-coil can also double as a pickup coil by detecting induction currents from a rotating magnetization in the sample.

2.2.1 Nuclear Magnetic Resonance

NMR is a type of spectroscopy which is based around the behavior of nuclear spins in a magnetic field. The different spin states of any nucleus in a magnetic field become non-degenerate and separate into slightly different energy levels[3]. As discussed in section 2.1, due to the thermal equilibrium dictating the spin state population, the higher energy levels are slightly less populated, thus leading to an overall magnetization M in the sample.

It is a useful visualization to picture each nuclear spin as a vector with a quantized nature, only allowing it to assume a discrete number of azimuthal angles towards B_0, corresponding to its allowed nuclear spin states. They can never perfectly align with the magnetic field and are required to have a certain angular momentum, as is evident from the Heisenberg uncertainty principle. The angular momentum may be understood as a precession of the nuclear magnetic dipole moment around the magnetic field axis. This phenomenon is called Larmor precession, and its rotational frequency ω_L is proportional to B_0 and the gyromagnetic ratio γ, which can in turn be understood as a ratio of the nuclear magnetic moment μ and the nuclear spin I:

$$\omega_L = -B_0\gamma = -B_0\frac{\mu}{I} \tag{2.6}$$

Because usually this precession movement is incoherent over all the spins of a sample, we cannot normally observe it directly on a macroscopic scale as a precession of the macroscopic magnetization vector M.

This changes when we expose the sample to a radio-wave with a frequency that resonates with the Larmor precession. The photon-energy then corresponds to the energy gap between the aforementioned nuclear Zeeman levels, thereby fulfilling the

[2]To be precise, B_1 only refers to half of the RF-waves magnetic field component. This will be explained in section 2.2.1.1.

[3]Referred to as the nuclear Zeeman levels.

resonance condition:

$$\Delta E = \hbar\omega_L = \gamma\hbar B_0 \tag{2.7}$$

Accordingly, if one scans either the frequency of the irradiated RF-wave or the strength of B_0 field over the resonance condition, one will measure an absorption line and a corresponding transversal RF-emission at the resonance condition. This is the procedure performed in a classical *continuous wave*-NMR (CW-NMR) experiment, which was the first and most straightforward type of NMR to be developed.

2.2.1.1 Use of Resonant Radiofrequency-Pulses

Instead of looking at the absorbed photons as a quantum phenomenon, one may also consider the effect of the B_1 field on the macroscopic magnetization in a classical description.

Consider the magnetic field component of the irradiated RF-wave to have an amplitude of $2B_1$ and oscillating along the x-axis of the samples coordinate system. Now consider this oscillation to be the superposition of two rotating magnetic fields overlapping, one of which is rotating in the same direction as the Larmor precession, the other one rotating with the opposite orientation. In this picture it is apparent that a consistent interaction between the precessing magnetic moments and the magnetic RF-field only happens with the magnetic field component rotating along the Larmor precession with the Larmor frequency. In this case, a resonant B_1 field will remain at a constant phase angle to the magnetization M, forcing it consistently further away from its equilibrium position along z.

Many sources also describe this in a coordinate system *x',y',z'* that is rotating along the precession with the Larmor frequency, in which case the movement of M due to the influence of B_0 takes a much simpler shape, as can be seen in figure 2.3.

The total azimuthal angle between M and z is proportional to both the amplitude of B_1 and the duration for which it is applied.

$$\theta_{pulse} = \gamma B_1 \tau_{pulse} \tag{2.8}$$

It is very often convenient to quickly change the magnetization by a flip-angle θ_{pulse} of either $\pi/2$ or π by applying a strong RF-field for an exactly calibrated duration.

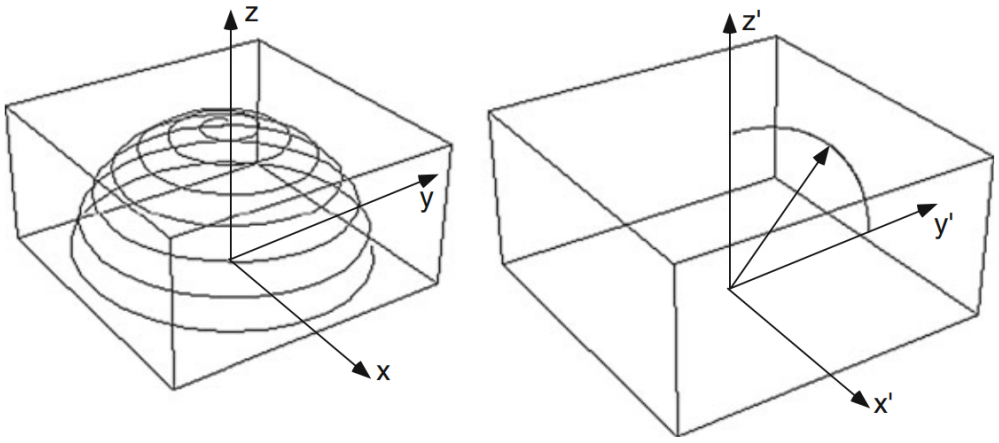

FIGURE 2.3: Motion of the magnetization vector **M** under the influence of the rotating magnetic field B1. The left side shows the laboratory coordinate system and the right side the rotating coordinate system. Figure adapted from [3].

RF-pulses that are designed for this purpose are referred to as $\pi/2$- or π-pulses respectively and are often used in specific sequences to manipulate the magnetization of the sample.

2.2.1.2 Relaxation

After an RF-pulse has turned the magnetization vector **M** away from its equilibrium position, it reverts back towards its equilibrium magnitude and relaxation in a process called relaxation. Splitting up the vector **M** in its components M_z, M_x and M_y, one generally differentiates between two types of relaxation. The *longitudinal* relaxation is the return of the M_z component towards equilibrum, while the transversal relaxation describes the recession of the M_x and M_y components. The relaxation process can be described using the *Bloch equations*:

$$\frac{dM_z}{dt} = -\frac{M_z - M_0}{T_1} \tag{2.9}$$

$$\frac{dM_{x'}}{dt} = \frac{M_{x'}}{T_2} \tag{2.10}$$

$$\frac{dM_{y'}}{dt} = \frac{M_{y'}}{T_2} \tag{2.11}$$

A more complex version of these equations that also describes the influence of a resonant B_1, describing the effect of resonant RF-pulses described in the previous section quantitatively, can be found in [3] or respective literature.

Solving these equations for the longitudinal relaxation yields an exponential decay towards the equilibrium magnetization with a decay constant T_1[4]. The longitudinal relaxation is often called the "spin-lattice" relaxation, because it is mainly caused by the interaction of polarized nuclei with their environment (in sold state this is often the crystal lattice) and describes the development of polarization in z-direction.
The transversal relaxation is also referred to as the "spin-spin" relaxation. One may picture it as a gradual dephasing of the initially coherent precession of the spins after a $\pi/2$-pulse. Once the phase coherence is totally lost, the overall magnetization projected on the xy-plane reaches zero. Since this relaxation is caused by different physical processes than T_1, it has a separate transversal relaxation constant T_2.
In a real sample, the natural dephasing of spins with T_2 is accelerated by inhomogeneities in the magnetic field that the nuclei of a sample experience. Such inhomogeneities can be either a fluctuation over time or in space and are caused by the chemical environment of the nuclei or imperfections in B_0. To differentiate this measured transverse relaxation from the true transverse relaxation time, it is referred to as T_2^*. This constant can also be seen as the "life-time" of the excited state caused by an absorbed RF-photon in the quantum physical picture.
The macroscopic magnetization rotating in the transverse plane constitutes a rotating dipole. As such, it acts as an antenna emitting radio-waves, which can be received by a suitable coil around the sample. For a single NMR-resonance, this signal takes the shape of a damped oscillation which is in amplitude proportional to the transverse relaxation, in frequency equal to the resonance frequency and has an envelope decaying exponentially with the constant T_2^*. This signal is called a Free Induction Decay (FID), and it is linked to the NMR-spectrum by a Fourier transformation.

[4]As will be described in the next section, hyperpolarization methods can produce magnetization that far exceed the equilibrium magnetization. In this case, one can solve the equations by approximating $M_0 = 0$. As a result, while in regular MR the longitudinal polarization "re-grows" after an RF-pulse, it keeps decaying towards the equilibrium value (close to 0) in hyperpolarized MR.

2.2.2 Magnetic Resonance Imaging

In the early 1970s, Paul C. Lauterbur developed a theory to use spatial gradients in the magnetic holding field in order to measure transversal relaxation times location-sensitively to create an image. Since human tissues exhibit different transversal relaxation times, such an image can differentiate between them, which allows this method, today known as Magnetic Resonant Imaging (MRI), to become one of the most powerful medical imaging tools to date.
The algorithms of MRI image acquisition have since developed and diversified greatly, but the general principles are common to all of them.
All MRI systems record induction decay signals similar to the above discussed FID signals. Magnetic field gradients are then used to differentiate between the induction signals generated at different locations in the sample. This is done in one of the three ways *selective excitation*, *phase encoding* or *frequency encoding*, which I will shortly discuss. Very often, these are also combined by using one type of encoding for each spatial dimension: One may, as a common example, record a three-dimensional image by selectively exciting a slice in z-direction, phase encoding the y-direction and frequency-encoding the x-direction.

2.2.2.1 Selective Excitation

This encoding method works by applying a magnetic field gradient during the initial $\pi/2$-pulse. The field gradient causes a different Larmor precession frequency throughout the sample. Since the RF-pulse can only rotate nuclei that meet the resonance condition into the transverse plane, all other spins in the sample will not be rotated or *excited*, i.e. they will not generate an induction signal.
Selective excitation is very commonly used with a $z-$gradient to achieve a *slice selection*.

2.2.2.2 Phase Encoding

To achieve a phase encoding, a field gradient is applied for a precisely defined duration in between the first $\pi/2$-pulse and the recording of the induction signal. During

the application of the gradient field, the transverse precession of the magnetization in the sample has a different angular velocity depending on its location in the sample. Therefore, the relative phase angle between the magnetization of neighboring locations will increase with strength and duration of the field gradient. Since induction signals with relative phase angles of π eliminate each other, a gradual change of the gradient field strength, and thereby the distance between a pair of spins whose signals eliminate each other, over many measurements can be used to extract the strength of transverse polarization at each point along the gradient direction. For more detailed description of the decoding mathematics, please consult [3] or respective literature.

Phase encoding is commonly used to resolve the y-direction in modern MRI systems. The Cates-Miller-Zheng (CMZ) algorithm that is used for the spatial resolution in this work also uses a type of phase encoding, although the details of the image reconstruction change due to the different nature of the detection scheme. See chapter 3.3 for a detailed description.

2.2.2.3 Frequency Encoding

Applying a field gradient during the acquisition of the induction signal results in a frequency encoding. This is mostly done in the $x-$direction and the gradient is sometimes referred to as a *readout gradient*.

Recording the induction signal under the influence of a readout gradient results in an increasing frequency of the induction signal of each voxel along the gradient direction. A Fourier transform of the received signal can therefore decrypt the spatial information.

2.2.2.4 Hyper-polarized Magnetic Resonant Imaging

Hyper-polarized (HP) MRI works in principle just like regular MRI, except that the achieved polarization through Spin-Exchange Optical Pumping(SEOP) is usually several orders of magnitude larger than polarizations achieved by the thermal equilibrium in a magnetic field at room temperature that is utilized by regular MRI. One other difference is that the effect of longitudinal relaxation is inversed. Regular

MRI destroys the longitudinal polarization using a $\pi/2$-pulse and then observes the longitudinal component of the magnetization re-grow from zero to its thermal equilibrium state, characterizing this relaxation with the time-constant T_1.
In HP-MRI, the SEOP generates a longitudinal magnetization that is many orders of magnitude larger than the thermal equilibrium state, and this magnetization slowly relaxes back to the equilibrium state[5].
Naturally, the practical differences by far exceed these principal ones, and the interested reader may refer to [10].

2.3 Polarisation by Spin-Exchange Optical Pumping

The field of Spin-Exchange Optical Pumping (SEOP) has grown in recent years due to its potential for HP-MRI.
In principle, the SEOP works by polarizing vaporized alkali-metal atoms through the interaction with circularly polarized laser-light. These atoms interact with noble gas atoms within the same gas mixture, thereby transferring their polarization to them.
While the technique works in principle with several alkali metals (^{133}Cs,$^{85}\,Rb$,$^{87}\,Rb$ and ^{39}K alone were tested in [11]) and noble gases (e.g. ^{3}He,$^{129}\,Xe$,$^{131}\,Xe$ and ^{83}Kr, [11–13]), in this work I will focus on the polarization of xenon isotopes using ^{87}Rb, which is an almost stable ($T_{1/2} = 4.97_{10}10\ y$) nucleus with an abundance in natural rubidium of close to 28%.
The overall mechanism of optical pumping on the rubidium atom, which I discuss in some detail below, is schematically depicted in figure 2.4.

2.3.1 Rubidium Polarization

The initial step of SEOP involves polarizing the *atomic* spins of the alkali metal vapor, in this case the ^{87}Rb. The ideal transition for this purpose is an excitation from the $5S_{1/2}$ state to the $5P_{1/2}$ state, known as the D1 absorption line. Photons

[5] Since the relaxation process is governed by a first-order differential equation, the time-constant of both types of relaxation is the same T_1, although the relaxation happens in the reverse direction and from a greater magnitude.

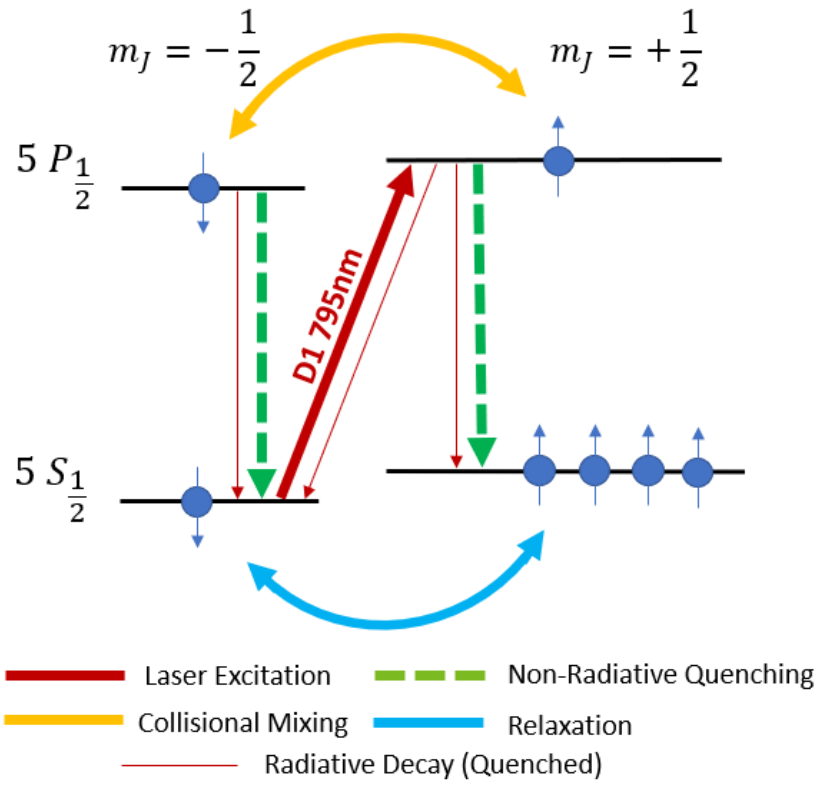

FIGURE 2.4: Illustration of the state transitions of rubidium atoms due to different processes during SEOP.

with a circular polarization carry an angular momentum. The polarization is denoted as σ^+ or σ^- depending on the direction of the angular momentum with respect to the propagation vector. While optical pumping works with both directions of circular polarization, we will focus on the case of σ^+ here for simplicity. Tuning a circularly polarized laser to the D1 absorption line of ^{87}Rb at 794.76569nm (in air, [14]), due to selection rules only allows electrons from the $5S_{1/2}$ state with $m_J = -1/2$ to be excited to the $5P_{1/2}$ with $m_J = +1/2$ by absorbing both the energy and angular momentum of the photon. In the $5P_{1/2}$ level, electronic spin of the rubidium atoms is exchanged with atoms and molecules of the buffer gases due to collisions[6]. The electron then decays back into one of the two Zeeman sub-levels of the $5S_{1/2}$ state with equal probability. If it does not decay back into the $m_J = -1/2$ state, such a cycle of excitation and consecutive decay results in a net polarization gain of $\Delta F = +1$ to the total atomic angular momentum F. Otherwise, the net

[6]This is such a dominant effect that both $5P_{1/2}$ states will be mixed thoroughly and can be considered [11, 12] to have the same population.

polarization gain is zero. Since both gases occur with 50% chance, a continuous irradiation with resonant σ^+ photons will eventually populate the $m_J = +1/2$ states while depopulating the $m_J = -1/2$ states, which constitutes a polarization of the rubidium atoms.

2.3.2 Radiation Trapping and Quenching

A problem of this polarization scheme is posed by the fluorescence photons emitted as a radiative decay from the $5P_{1/2}$ state, which are generally unpolarized, but naturally tuned to the D1 line. That means that they trigger the same cycle of absorption and emission. However, since they do not carry a circular polarization, they can also excite electrons from the $m_J = +1/2$ state. If the rubidium is already somewhat polarized, this is more likely than excitation from the $m_J = -1/2$ state, since the former has a higher population. Yet, the likelihood of the decay back into the the $m_J = +1/2$ state is still only 50%, so that the net effect of this cycle is the de-population of the $m_J = +1/2$ state toward equilibrium and therefore the de-polarization of the system. This effect to is referred to as "radiation trapping" [12].

The problem can be mitigated by adding nitrogen gas into the polarization cell. The triple bonded nitrogen molecules exhibit vibrational modes that can, during collisions between the rubidium atom and the nitrogen molecule, absorb the energy of the $5P_{1/2}$ state without the emission of a photon. At high partial pressures of nitrogen, this "quenching" mechanism dominates over the radiative decay and thereby mitigates de-polarization effects from fluorescent photons.

2.3.3 Spin Exchange

Spin exchange between the rubidium and other gases happens through two distinct physical processes, which are binary collisions and short-lived Van-der-Waals molecules between Rb and Xe. Details on these processes have covered thoroughly in [11]. Here it shall be sufficient to note that the overall spin exchange rate γ_{SE} is especially at low xenon concentrations dominated by the spin exchange during the

life-time of Van-der-Waals molecules[7] (we denote the rate as γ_{RbXe}) as opposed to the exchange rate $\langle \sigma v \rangle$ through binary collisions.

$$\gamma_{SE} = [Rb] \left(\frac{\gamma_{RbXe}}{[Xe]} \cdot \frac{1}{1 + b\frac{[N_2]}{[Xe]}} + \langle \sigma v \rangle \right) \tag{2.12}$$

Here, b is a constant called the *characteristic pressure* (values found in [15]) and the gas pressures $[Rb], [Xe]$ and $[N_2]$ are given as number densities, i.e. the number of individual molecules or atoms per cubic meter.

2.3.4 Optical Pumping Rate Equations

The process of SEOP can be quantitatively described using rate equations with pumping and relaxation rate parameters that can be measured for different gas pressures and mixtures. Here, I show the rate equations as presented in [12]. The first rate equation describes the polarization P_{Rb} of the alkali metal, in our case the rubidium:

$$P_{Rb} = \frac{\gamma_{op}}{\gamma_{op} + \gamma_{trap} + \sum_i \kappa_{sd}^i [M_i]} \tag{2.13}$$

Here, γ_{op} represents the rate of optical pumping, i.e. the rate at which laser light is absorbed by the rubidium, γ_{trap} is the depolarization rate through radiation trapping effects and the different spin destruction rates κ_{sd} (values listed in [15]) describe the depolarization rates through binary collisions. Here one should note that the polarization transfer in collisions with nitrogen is nearly three orders of magnitude smaller than the transfer to noble gases and five orders of magnitude smaller than in collisions with other rubidium atoms.

Knowing this in combination with the spin exchange rate γ_{SE}, one may proceed to calculate the consecutive noble gas polarization P as a function of the polarization time t_{pol}:

$$P(t_{pol}) = \frac{\gamma_{SE}}{\gamma_{SE} + \Gamma} P_{Rb} (1 - e^{-(\gamma_{SE} + \Gamma) t_{pol}}) \tag{2.14}$$

[7] This process becomes less dominant at higher xenon concentrations because collisions between such a Van-der-Waals molecule and a xenon atom is likely to destroy the molecule. Therefore, high xenon densities shorten the average life-time of these molecules an thereby limit the spin exchange rate through this process. Collisions with nitrogen molecules are much less likely to destroy a the Van-der-Waals molecule [12].

Here, Γ describes the reciprocal longitudinal "self"-relaxation time of xenon, i.e. $\Gamma = \frac{1}{T_1}$. It is apparent that as time increases and $(\gamma_{SE}+\Gamma)t_{pol} >> 1$, a maximum "steady-state" polarization is reached. Once this polarization of the electron spins of the xenon atoms is achieved, hyperfine coupling processes also transfer this polarization to the xenon nucleus[8], thereby creating the nuclear polarization required for the gamma-MRI method.

[8]Strong magnetic fields are able to decouple nuclear and electron spins, which should be taken into consideration when performing the optical pumping within the measurement magnet.

Chapter 3

Method

The imaging method that we call *gamma-MRI* in this work was first introduced under the term *Polarized Nuclear Imaging* by *Y. Zheng et al.* in [1, 13]. In this work we present our own dedicated design to perform similar studies and expand on the published findings. The following sections will summarize the gamma-MRI method.

3.1 General Setup

The principal geometry of a gamma-MRI setup is illustrated in figure 3.1. The entire setup is situated within the magnetic holding field B_0. In this illustration, the sample in the center is polarized by the laser at the same location where the MR-measurement takes place between RF-coils and gamma-detectors, although in principle, polarization and measurement may be separated in time and space.

3.1.1 Radiation from Aligned ^{131m}Xe Nuclei

At the core of the setup, we find the sample. In both the experiments performed by *Y. Zheng et al.*, as well as the ones described in this work, the sample consists of a gas phantom with trace quantities of ^{131m}Xe. I will refer to the container holding the glass phantom as the *target vial*. This isomer exhibits a gamma emission of

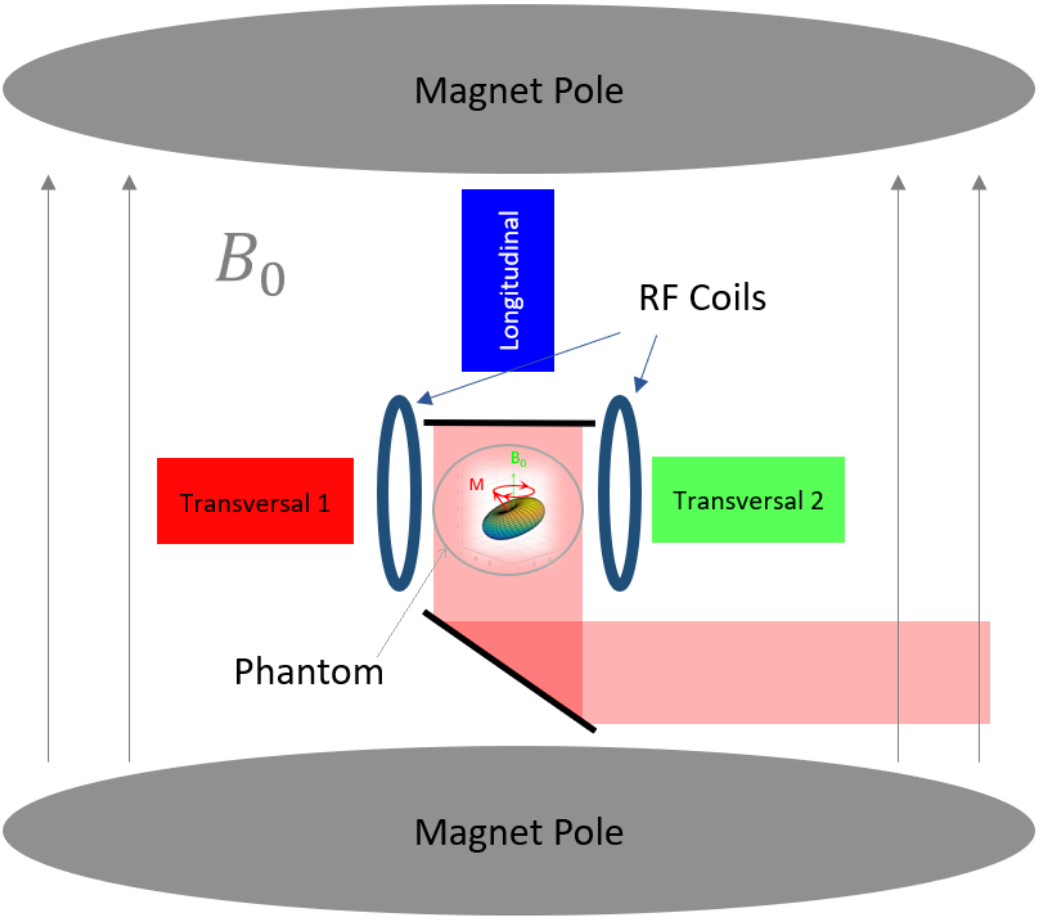

FIGURE 3.1: Simplified schematics of a gamma-MRI setup. Gradient coils are omitted for simplicity.

163.93keV photons when decaying from the isomeric state into the ground state. The isomeric state has a half-life of 11.84 days and a spin of $11/2-$, decaying via an M4-transition to the 3/2 ground state. When polarized, this transition has a strong anisotropic emission behavior. The relevant angular distribution coefficients (c.f. eq. 2.5) are $A_2 = -0.88902$, $A_4 = 0.44341$, $A_6 = 0.032$ and $A_8 = 0.2624$, as calculated with the Anisotropy Tool described in section 4.1, which is in agreement with tabulated values from [2, 16][1]. The higher orders of A_λ are zero.

This xenon is hyper-polarized via SEOP by the laser irradiating it. In general, equation 2.5 describes the directivity of its gamma-emissions. For the practical application, a few simplifications can be made. For one, the parameters U_λ can be

[1]When looking at the tabulated values, these A_λ coefficients are tabulated as F_λ, because A_λ may in general also describe mixed transitions (e.g. E2+M4) which can be calculated from several sets of F-coefficients. Since the transitions considered in this work are pure transitions, we can work with $F_\lambda = A_\lambda$.

neglected, since there is no intermediate radiation between polarization and emission. G_λ will be depicted by the MR relaxation formalism. We are therefore left with:

$$W(\theta) = 1 + B_2 A_2 P_2(\cos(\theta)) + B_4 A_4 P_4(\cos(\theta)) + B_6 A_6 P_6(\cos(\theta)) + B_8 A_8 P_8(\cos(\theta)) \tag{3.1}$$

Since it is advantageous for the following mathematics, *Y. Zheng* suggests in [13] to write equation 3.1 in the form of

$$W(\theta) = a_0 + a_2 \cos(2\theta) + a_4 \cos(4\theta) + a_6 \cos(6\theta) + a_8 \cos(8\theta) \tag{3.2}$$

While not finding an analytical relation between a_λ and A_λ (which seems to be implied in [13]), equation 3.2 is effectively a Fourier series expansion of equation 3.1, which is by definition possible because the function in equation 3.1 is periodic. Finding the parameters a_λ using a numeric least-squares algorithm, it could be confirmed that the Fourier expansion terminates at the same order as the original form and does not require uneven orders of λ. Since for achievable degrees of polarization, a_6 and a_8 are very small compared to a_2 and a_4 [13], we will in the following considerations often neglect the higher order terms.

3.2 The Detector Count-Rates

In the configuration illustrated in figure 3.1 it is apparent[2] that, as soon as the radioactive xenon nuclei in the sample become aligned, the count rates of the longitudinal and transversal detectors will change. Let us first consider the partial count rate dR of a point-shaped sample at location $\mathbf{r_s}$ with a magnetization direction $\hat{\mathbf{M}}$ and an infinitesimally small detector with an surface area dA_d, situated at a location $\mathbf{r_d}$, facing in the direction $\hat{\mathbf{n}}_\mathbf{d}$. In this case we can define the count-rate dR of the

[2] Please consider for reference the angular distribution function plotted in figure 2.2.

detector surface element dA based on:

$$\mathbf{r}_\gamma = \mathbf{r_d} - \mathbf{r_s} \tag{3.3}$$

$$\theta_{eff} = \angle(\hat{\mathbf{M}}, \mathbf{r}_\gamma) \tag{3.4}$$

$$\alpha = \angle(\hat{\mathbf{n}}_\mathbf{d}, \mathbf{r}_\gamma) \tag{3.5}$$

$$dR = CW(\theta_{eff})\cos(\alpha)dA \tag{3.6}$$

C is a constant that describes the activity of the sample and detector efficiency, as well as absorption on the path, neglecting the weak spatial dependence of the latter. Figure 3.2 illustrates this consideration.

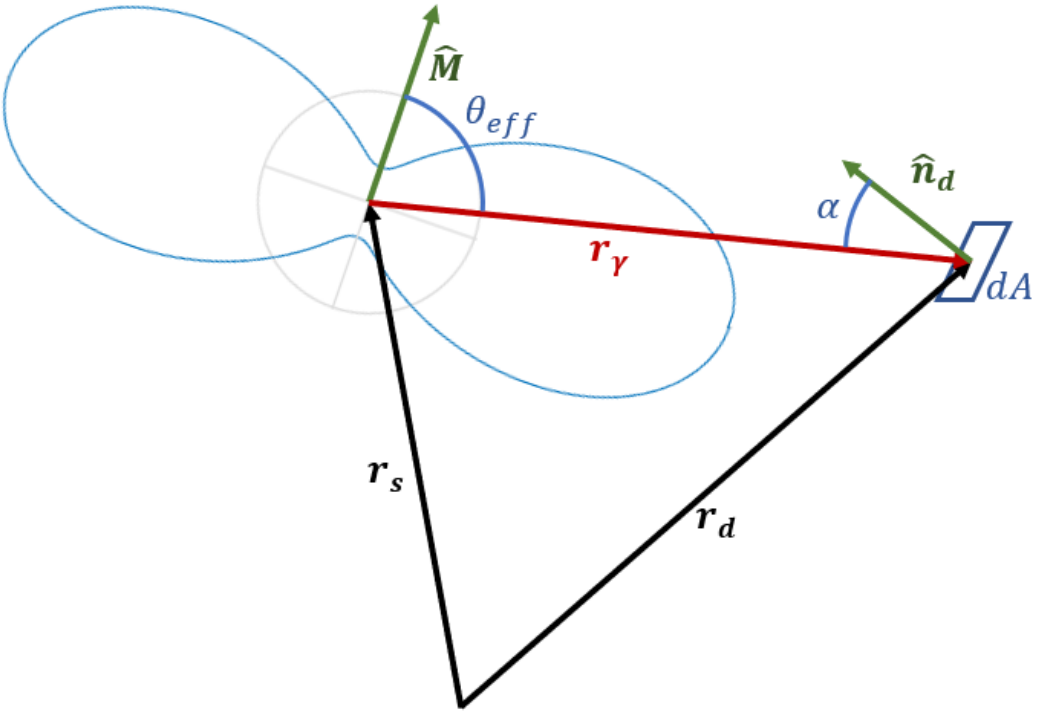

FIGURE 3.2: Illustration of point-sized polarized sample and its relation to a detector element.

For an extended detector and sample with a density $\rho(\mathbf{r})$ of the radioactive tracer, we will find:

$$R = C\int_{V_{Sam}}\int_{S_{Det}} \rho(\mathbf{r})W(\theta_{eff})\cos(\alpha)dAd\mathbf{r} \tag{3.7}$$

It is well to keep in mind that, unless the magnetization is parallel to the z-axis, it will precess around the latter with the Larmor frequency, as is illustrated in

subfigure 2.2b. In this case, θ_{eff}, and with it the whole count-rate, will become time-dependent. Equation 3.7 is solved numerically in the *PNI Simulation* script.

Let us now consider the important special cases of detectors located longitudinal (i.e. along the z-axis) and transversal (i.e. on the xy-plane) to the direction of polarization. For the longitudinal detector, the precessing motion of $\mathbf{M}$ does not alter θ_{eff}, so that the count-rate remains time-independent. A transversal detector however sees a maximal modulation in its count-rate during the precession. If θ_0 is the polar and $\phi(t) = \omega_L t$ the azimuthal angle of $\hat{\mathbf{M}}$, the θ_{eff} for a detector along the x-axis will be:

$$\cos(\theta_{eff}(t)) = \sin(\theta_0)\cos(\omega_L t) \tag{3.8}$$

To simplify further, we will assume that the z-component of the magnetization is zero[3], so that $\sin(\theta_0 = \pi/2) = 1$ and $\theta_{eff} = \omega_L t$. Further, the detector normal vector $\hat{\mathbf{n}}_\mathbf{d}$ is aligned to the source so that $\cos(\alpha = 0) = 1$. Now we can combine equations 3.23 and 3.8:

$$R_{trans} = C \int_{V_{Sam}} \int_{S_{Det}} \rho(\mathbf{r})[a_0 + a_2\cos(2\omega_L t) + a_4\cos(4\omega_L t)]dAd\mathbf{r} \tag{3.9}$$

It is worth noting that this transversal detector will see two oscillations in the count-rate, one with a frequency of $2\omega_L$ and an amplitude proportional to a_2, as well as one with a frequency of $4\omega_L$ and an amplitude proportional to a_4.

3.3 Phase Encoding in gamma-MRI

A specially developed phase encoding pulse sequence was introduced by and named after [1, 13] *Cates, Miller and Zheng* (CMZ-sequence).
To understand this sequence, let us consider the effect of applying a gradient magnetic field $\mathbf{G}$ for a time τ after tipping the spins into the transverse planes by using a $\pi/2$ pulse.

$$\mathbf{G} = (\partial B_z/\partial x)\hat{\mathbf{x}} + (\partial B_z/\partial y)\hat{\mathbf{y}} \tag{3.10}$$

[3] As would be the case after a $\pi/2$-pulse.

As mentioned above, the azimuthal angle of a tipped spin without a gradient field has a time-dependence of $\phi(t) = \omega_L t$. Combining this with definition of the Larmor frequency, we get an angle of ϕ_f:

$$\phi(t) = -B_z \gamma t \tag{3.11}$$

$$\phi_f = -\gamma(B_0 t + \tau \mathbf{G} \cdot \mathbf{r}) \tag{3.12}$$

At a defined point in time after this first pulse, we apply a second $\pi/2$-RF pulse. The effect is again to tip the magnetization around the y-axis by 90°, but this time, starting in the transverse plane and from an azimuthal angle ϕ_f. Let this be described in a matrix operation:

$$\hat{\mathbf{M}}_0 R_y = \hat{\mathbf{M}}_1 \tag{3.13}$$

$$\begin{pmatrix} \cos(\phi_f) \\ \sin(\phi_f) \\ 0 \end{pmatrix} \begin{pmatrix} 1 & 0 & 0 \\ 0 & 0 & -1 \\ 0 & 1 & 0 \end{pmatrix} = \begin{pmatrix} \cos(\phi_f) \\ 0 \\ \sin(\phi_f) \end{pmatrix} \tag{3.14}$$

Transforming the resulting $\hat{\mathbf{M}}_1$ back to polar coordinates, we get a new polar angle of

$$\theta_f = \cos^{-1}(\sin(\phi_f)) = \pi/2 - \phi_f \tag{3.15}$$

While at this point the precession motion of the spins proceeds naturally, this polar angle remains constant. This also means that, as mentioned in section 3.2, the count-rate of a longitudinal detector remains time independent.

$$R = C \int_{V_{Sam}} \int_{S_{Det}} \rho(\mathbf{r}) W(\theta_{eff}) \cos(\alpha) dA d\mathbf{r}, \tag{3.16}$$

where

$$W(\theta_{eff}) = W(\theta_f) \tag{3.17}$$

$$= W(\pi/2 - \phi_f) \tag{3.18}$$

$$= W(\pi/2 + \gamma(B_0 t_d + \tau \mathbf{G} \cdot \mathbf{r})) \tag{3.19}$$

and t_d shall denote the time[4] between two RF-pulses. For the following considerations, we will also omit the weak spatial dependence that is introduced by the integration over the detector area $\int_{S_{Det}} \cos(\alpha) dA$, assuming it to only modify the constant C, so that we can simplify to

$$R = C \int_{V_{Sam}} \rho(\mathbf{r}) W(\pi/2 + \gamma B_0 t_d + \gamma \tau \mathbf{G} \cdot \mathbf{r}) d\mathbf{r} \tag{3.20}$$

This equation tells us that the count-rate in the longitudinal detector after two $\pi/2$-pulses encodes information about the overall phase angle ϕ_f that was covered in the precession motion in the transverse plane during t_d, while a gradient field that is applied for a duration τ adds spacial information to this phase.

3.4 Image Reconstruction

This can be used to design pulse sequences that allows a full image reconstruction. First, let us choose a delay time between the two pulses that corresponds to a half integer multiple of the Larmor period $\tau_L \equiv 2\pi/(\gamma B_0)$:

$$t_d = n \frac{\tau_L}{2} \tag{3.21}$$

With that, the inclination angle after the two pulses used in equation 3.19 can be written as:

$$\theta_f = \pi/2 + n\pi + \gamma \tau \mathbf{G} \cdot \mathbf{r} \tag{3.22}$$

Now we consider the zeroth and second order terms of equation 3.2,

$$W(\theta) \simeq a_0 + a_2 \cos(2\theta) \tag{3.23}$$

and simplify after inserting θ_f, so that:

$$W_R(\theta_f) \simeq a_0 - a_2 \cos(2\gamma \tau \mathbf{G} \cdot \mathbf{r}) \tag{3.24}$$

[4]Defined between the onset of both pulses. Ideally, RF pulses are chosen with high intensity and short duration, so that $t_{pulse} \ll t_d$.

At this point, we can define a **k**-space vector similar to that in regular MRI:

$$2\pi\mathbf{k} \equiv 2\gamma\tau\mathbf{G} \tag{3.25}$$

Combining equations 3.25, 3.24 and 3.20, we can describe the count-rate after the double pulse as a function of **k**-space location

$$S_R = C\int_{V_{Sam}} \rho(\mathbf{r})[a_0 - a_2\cos(2\pi\mathbf{k}\cdot\mathbf{r})]d\mathbf{r} \tag{3.26}$$

Zheng et al. [1] named the quantity S_R the sample's *real spin moment.*, because it is used in the image-reconstruction as the real part of the complex spectrum.
The value of the corresponding imaginary part is measured by another double-pulse sequence, however with a delay time between the pulses that is 1/8 of a Larmor period longer, i.e.:

$$t_d = (n + 1/4)\frac{\tau_L}{2} \tag{3.27}$$

In the same way in which we arrived at equation 3.24, we calculate

$$W_I(\theta_f) \simeq a_0 + a_2\sin(2\gamma\tau\mathbf{G}\cdot\mathbf{r}), \tag{3.28}$$

so that the *imaginary spin moment* can be written as:

$$S_I = C\int_{V_{Sam}} \rho(\mathbf{r})[a_0 + a_2\sin(2\pi\mathbf{k}\cdot\mathbf{r})]d\mathbf{r} \tag{3.29}$$

Once both real and imaginary spin moments are measured for each point of the k-space, one can construct their complex sum as

$$S_R + iS_I = C\int_{V_{Sam}} \rho(\mathbf{r})W_R(\mathbf{k},\mathbf{r})d^3r + C\int_{V_{Sam}} \rho(\mathbf{r})W_I(\mathbf{k},\mathbf{r})d^3r \tag{3.30}$$

$$:= A_0 - A(\mathbf{k}) \tag{3.31}$$

and simplify it (please refer to appendix B for a detailed calculation) using the definitions

$$A_0 = Ca_0(1+i)\int_{V_{Sam}} \rho(\mathbf{r})d_3r \tag{3.32}$$

$$A(\mathbf{k}) = Ca_2\int_{V_{Sam}} \rho(\mathbf{r})e^{-i2\pi\mathbf{k}\cdot\mathbf{r}}d_3r \tag{3.33}$$

in order to reconstruct the distribution of the emitting nuclei ρ by means of the Fourier transform

$$\rho(\mathbf{r}) = \frac{1}{Ca_2}\int_{V_k} A(\mathbf{k})e^{2\pi i\mathbf{k}\cdot\mathbf{r}}d_3k, \tag{3.34}$$

where $A(\mathbf{k}) = A_0 - (S_R + iS_I)$.

The resulting pulse CMZ sequence and the correlated detector count-rates are plotted in figure 3.3. The spin moment is the integrated count-rate of the longitudinal detector during the "gamma acquisition" period.[5] For the mathematics of deriving the spin moments from the transversal detectors, please consult [1].

[5]The careful reader might notice the oscillation of the longitudinal detectors count-rate during the "gamma acquisition" duration, which should not be present for a longitudinal detector according to the mathematics described above. This appears because the detector is spatially extended and therefore always records a small component of the transverse asymmetry. Simulating a detector without spatial extension is possible and removes this oscillation.

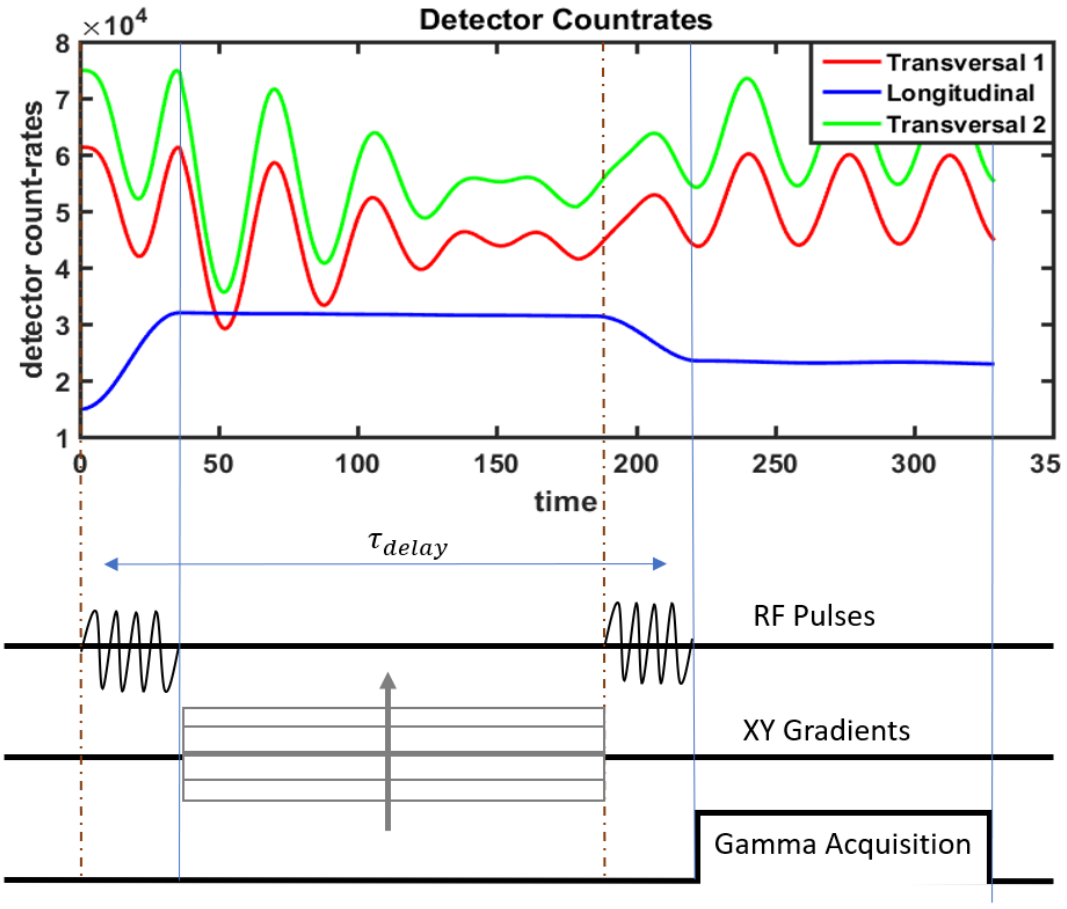

FIGURE 3.3: Detector count-rates during a CMZ-pulse sequence, as calculated with the gamma-MRI simulation software discussed in section 4.2.

Chapter 4

Software and Simulation

In order to calculate and visualize the various expectations from the planned experiments, several simulations have been performed using the MATLAB language and environment.

4.1 Anisotropy Tool

It became quickly apparent that a detailed understanding of the directivity of radiation depending on the possible m-state populations would be necessary. For this reason, a script including a graphical user interface (GUI) was created in order to calculate the correct parameters for the numeric calculation of equation 2.5. With the relative m-states populations of the mother nucleus as input, the tool is also able to simulate a chain of up to four consecutive decays, simulating the *orientation parameters* B_λ for each intermediate state as well as the *angular distribution* A_λ and *deorientation coefficients* U_λ for each transition.
The GUI is depicted in figure 4.1. The code calculates the relevant coefficients based on those found in [2]. The most important ones are:

$$B_\lambda(I_0) = \hat{\boldsymbol{\lambda}}\hat{\mathbf{I}}_0 \sum_m (-1)^{I_0+m} \begin{pmatrix} I_0 & I_0 & \lambda \\ -m & m & 0 \end{pmatrix} p(m) \tag{4.1}$$

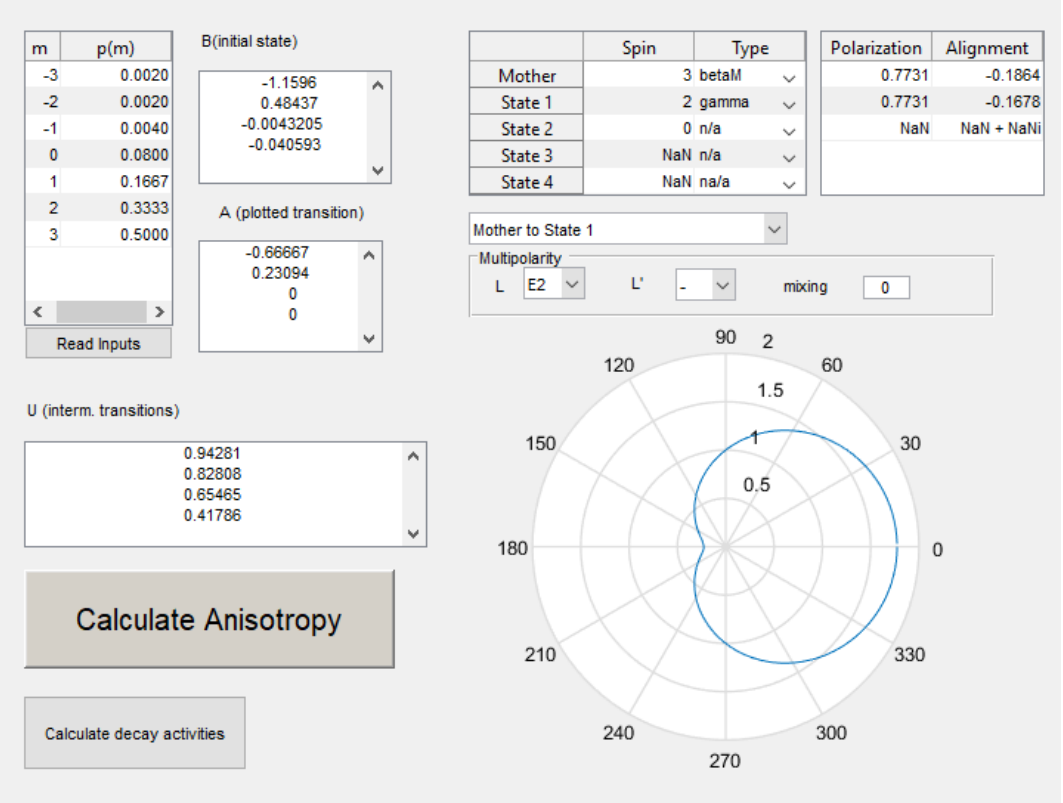

FIGURE 4.1: Graphical interface of the anisotropy tool. The values describe a strongly polarized nucleus with $I = 3$, decaying in a β^--decay to a $I = 2$ nucleus, which in turn emits a gamma-photon while dropping to $I = 0$. The dropdown-menu selection causes the polar plot to display the angular distribution of the initial β^--decay.

$$U_\lambda(I_1 I_2 L) = (-1)^{I_1+I_2+L+\lambda} \hat{\mathbf{I}}_1 \hat{\mathbf{I}}_2 \begin{Bmatrix} I_1 & I_1 & \lambda \\ I_2 & I_2 & L \end{Bmatrix} \tag{4.2}$$

$$A_\lambda(\gamma) = \frac{F_\lambda(LLI_fI_i) + 2\delta F_\lambda(L'L'I_fI_i) + \delta^2 F_\lambda(LL'I_fI_i)}{1+\delta^2} \tag{4.3}$$

With δ referring to the *multipole mixing ratio* and

$$F_\lambda(LL'I_fI_i) = (-1)^{I_f+I_i+1} \hat{\boldsymbol{\lambda}} \hat{\mathbf{L}} \hat{\mathbf{L}}' \hat{\mathbf{I}}_i \begin{pmatrix} L & L' & \lambda \\ 1 & -1 & 0 \end{pmatrix} \begin{Bmatrix} L & L' & \lambda \\ I_i & I_i & I_f \end{Bmatrix} \tag{4.4}$$

The matrices in round brackets represent Wigner 3-j symbols and those in curly brackets denote Wigner 6-j symbols. $p(m)$ is the probability of the m-state to be populated. The tool cannot calculate transitions that mix more than two multipolarities. For beta-decays, the anisotropy tool can only treat allowed decays, i.e. $I_i - I_f = 0$ (Fermi decay) or $I_i - I_f = \{0, \pm 1\}$ without parity change (Gamow-Teller

decay). For these transitions, only the first order coefficients are important and the angular distribution is described by

$$W_{\beta^{\pm}}(\theta) = 1 \mp \frac{2}{3}\frac{v}{c}F_1(11I_fI_i)U_\lambda B_1(I_i)cos(\theta), \tag{4.5}$$

where the v/c-term is approximated with 1, since most beta particles are emitted at speeds very close to the speed of light.

4.2 gamma-MRI Simulation

In order to understand and optimize the pulse sequences and algorithms that lead to the gamma-MRI Image, an object-oriented simulation was created.
The "world" of the simulation program is plotted in figure 4.2. Here, a cubic sample is surrounded by three detectors. The `sample` is represented by a number (in this case 4x4x4) of `voxels`, which are each plotted with a red magnetization vector and a surface plot representing their angular emission behavior, equivalent to the plot in figure 2.2b.

The detectors are in turn split into smaller elements that called `sensors` (to avoid confusion with the 'pixels' of the reconstructed MRI image). Each `voxel` is connected to every `sensor` with a `ray`. In principle, the simulation models the time-evolution of all `voxels` as well as their angular emission distribution to find the `intensity`[1] of each `ray` and in turn the count-rates of the `detectors`. Each `voxel` is a logic object representing one assembly of nuclei at a certain point in space with a certain magnetization vector and a certain `activity`[2], which may also experience varying magnetic fields (e.g. due to B_0-gradients).
The `voxel` class includes another method `voxel.evolve()` that simulates the natural evolution of the magnetization over time due to relaxation processes. While initial simulations represented the spin-flipping due to RF-pulses using a simple rotation matrix, it became clear that a detailed understanding of the RF-sequence and its effects would be crucial. Therefore, the method `voxel.RFevolve()` expands the

[1] Which is the average number of photons that would be emitted from `voxel` X in the direction of sensor X per second, calculated each simulation time-step.
[2] I.e. an amount of photons emitted by the represented ensemble of nuclei each second.

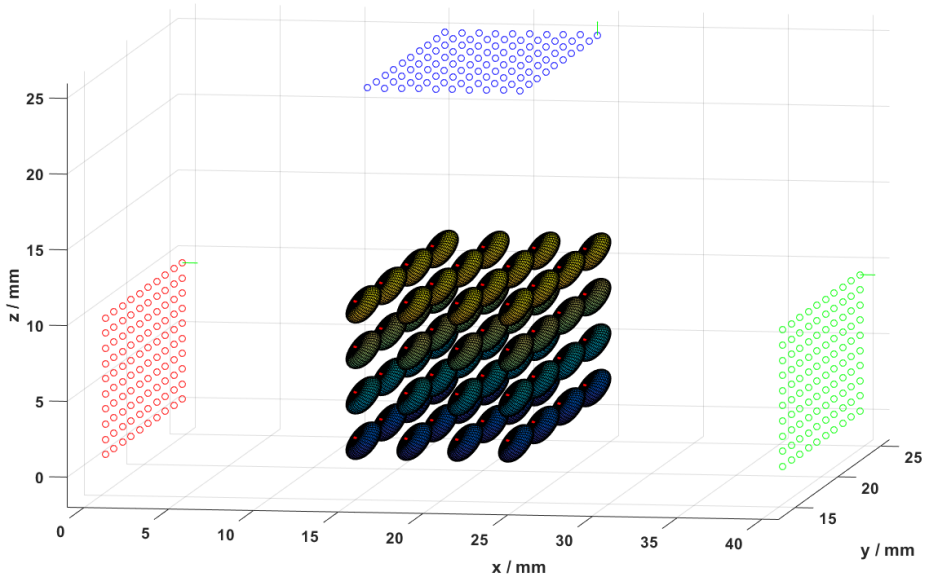

FIGURE 4.2: Plot of a simple gamma-MRI simulation. In this example, three detectors with each 10x10 sensors are located around a sample of 4x4x4 voxels, each represented by a red vector indicating its direction of magnetization and a surface plot visualizing the directional distribution of its radiation, just like in figure 2.2b. The ray vectors are not visible in the plot, but one ray connects each voxel to each sensor.

capability of `voxel.evolve()` to simulate the evolution under the influence of transverse RF-fields. This is done by a direct numerical solution to the Bloch equations. As demonstrated by reproducing a measurement from [13] (see appendix A), the simulation is can accurately predict the spin precession and rotation under magnetic gradients and RF-pulses. However, the correct settings for the gradients which determine the sampling of the k-space and therefore the image reconstruction still contain errors, leading to incorrect reproduced images. Hopefully, this can be corrected soon.

4.2.1 The 'Simulation' Script

Since this simulation is designed as a foundation to simulate many different scenarios rather than a specific one with different parameters, it is not suited to be integrated into a GUI, but held in form of a script. The code of this script is presented in appendix C. In order to help understanding the developed code, the main functionalities of `Simulation.m` are summarized here.

The first section of code is dedicated to setting input parameters that remain constant during run-time. Some of the most important ones are listed in table 4.1.
The next code sections *Make detector* and *Make sample* call constructors of the `detector` and `sample` classes, allocating them a number of their respective subclasses (`sensor`s and `voxel`s) spaced equally within specifiable limits. The "samples" that are created in this way are generally simple cuboid consisting of $N_x \times N_y \times N_z$ `voxel`s with a homogeneous distribution of tracer activity in each voxel. More complex structures can be generated by modifying the activity of the voxels afterwards. The spatial limits passed to the *detector* constructor should, as one may expect, be specified so that the resulting detector forms a plane of *sensors*, representing the surface of a real detector.
The following *Prepare Image* code section directly reads the spatial distribution of radioactivity in the generated *sample* and calculates the Fourier transform, in order to create an ideal reference image to compare the simulated image to.
Now follows the *Measurement Sequence* section, which executes the RF pulse sequence and records detector counts. I have implemented three pulse sequences of interest:

1. A simple single-pulse sequence that shows spin precession after an RF-pulse pulse of variable duration,

2. a delay-scan sequence that tests if the magnetization behaves as predicted by the formalism described in chapter 3, by gradually increasing the t_{delay} between two $\pi/2$-pulses and recording count-rates afterwards, and

3. a full CMZ sequence including image reconstruction.

After the pulse sequence part has run, the last section delivers final plots, although many plotting options are available up to this point in the simulation.

[3]This parameter is multiplied with the orientation parameters, which has the same effect on the angular distribution of radiation as a Gaussian distributed dephasing of spins.
[4]For measuring the real spin moment.

TABLE 4.1: Important input parameters within the gamma-MRI simulation script.

Variable	**Description**	**Type**	**Unit**
`dt`	Simulation timestep	double	s
`T1`	Longitudinal relaxation time	double	s
`T2`	Transversal relaxation time T_2^*	double	s
`activity`	Overall sample activity	double	Bq
`voxdistance`	"voxel" size	double	mm
`B_hold`	Constant magnetic field B_0	double	T
`Sample_xlimits`	Spatial limits for cuboid sample. Analogous parameters for y and z. $[min; max]$	(2x1)double	mm
`gradients`	Maximum gradient field strength $[\partial B/\partial x; \partial B/\partial y; \partial B/\partial z]$	(3x1)double	T/mm
`A`	Angular distribution coefficients $[A_2; A_4]$	(2x1)double	-
`B`	Orientation parameters $[B_2; B_4]$	(2x1)double	-
`polarization`	Factor representing reduced (initial) polarization[3]	double	-
`gamma`	Detection probability of detector	double	-
`det_prob`	Distance between sensors within detector	double	mm
`t_del`	Delay between RF pulses during CMZ sequence[4]	double	s
`t_grad`	Duration for witch gradients are active during CMZ sequence	double	s

Chapter 5

Extracting Xenon From Iodine

The key element of the gamma-MRI modality is the use of a radioactive tracer nucleus. Since this work is built on the proof of principle shown by [1, 13] and expands on those successes, we have chosen to also use ^{131m}Xenon. However, due to the

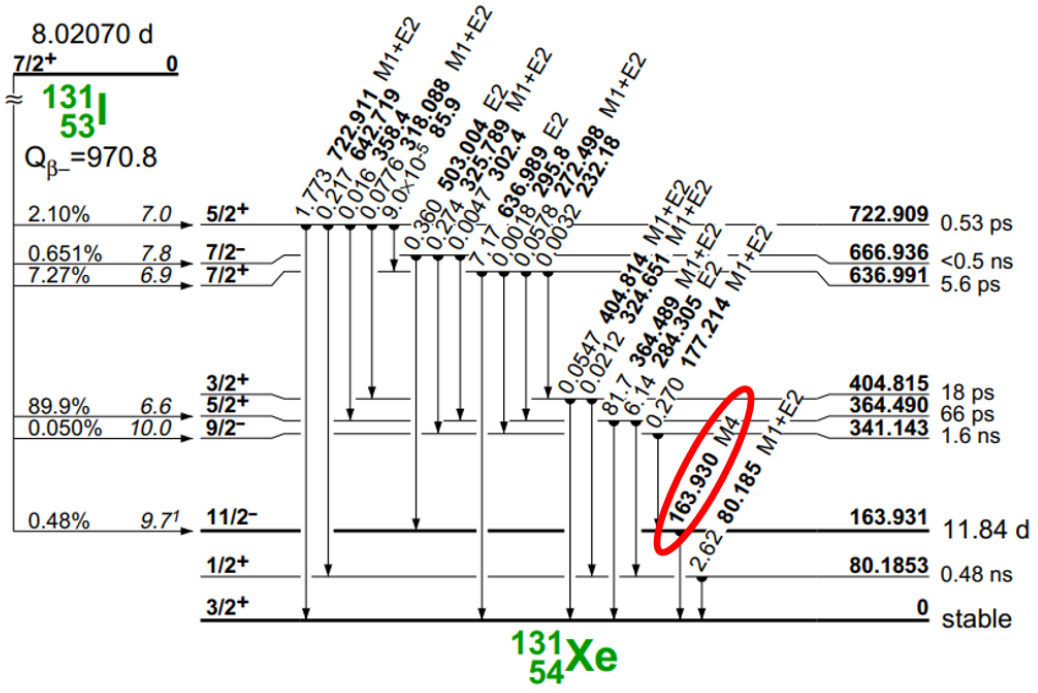

FIGURE 5.1: Iodine to Xenon decay scheme [4] with a red highlight on the radiation from the ^{131m}Isomer to the ground state, which is relevant for the gamma-MRI method.

isotope production capabilities provided by ISOLDE, we also have the option of ^{133m}Xenon, which has very similar properties. Unlike *Zheng et al.*, we where not

able to find ^{131m}Xenon commercially available, which is usually obtained as a decay product of ^{131}Iodine. Still, a production as a decay product is a good alternative to a direct production at ISOLDE. It is also desirable to have a source of radioactive iodine available during the upcoming long shutdown period (2019-2020) of CERN. Therefore it was decided to build a setup capable of extracting ^{131m}Xenon directly from a source of ^{131}Iodine in liquid solution, which is widely used as a medical tracer and readily available, since it is produced as a byproduct in nuclear power plants and research nuclear reactors.

This availability makes it attractive in nuclear medicine despite its hazardous properties from a radiation protection perspective. Pure Iodine at room temperature is generally liquid, but highly volatile, so large quantities tend to evaporate into air and condense on many surfaces. When such volatile radioactive iodine is inhaled, large quantities can condense in the thyroid, leading to a high risk of cancer. The distribution of iodine pills (which work by saturating the thyroid with non-radioactive iodine in order to prevent the absorption of radioactive iodine) after nuclear accidents is due to this property. Due to its common usage in nuclear medicine, many studies

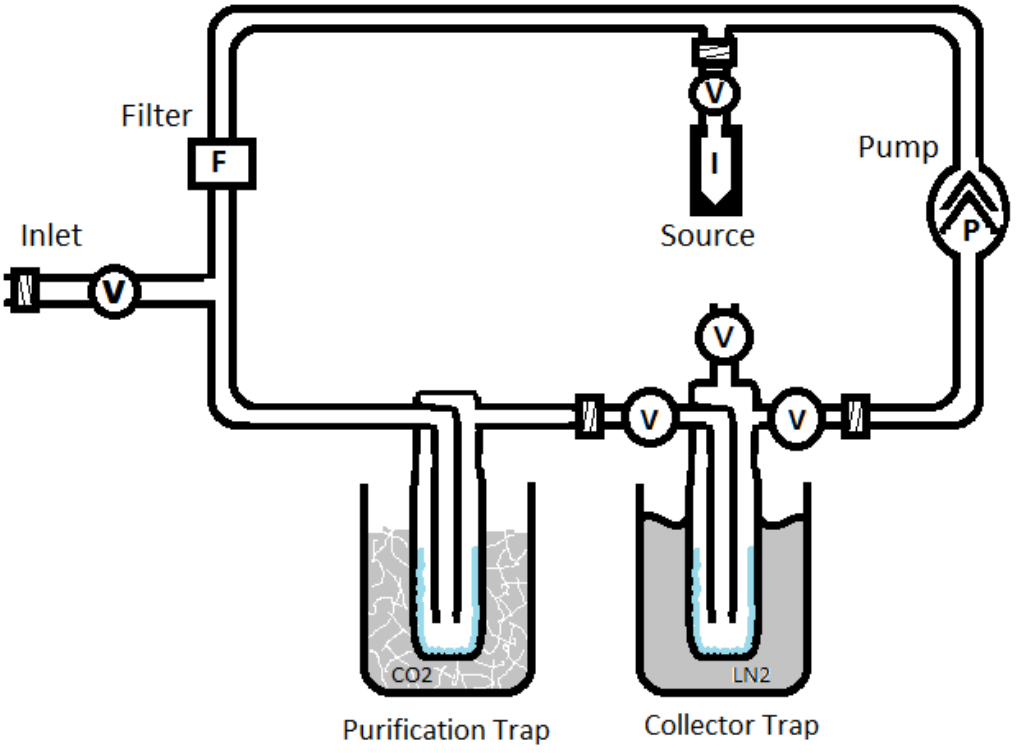

FIGURE 5.2: Concept of the decay loop setup.

[17, 18] have been devoted to its volatility in air and consecutive hazardousness for the administering personnel. Following these studies, radiation protection protocols are extremely strict for radioactive iodine, especially when present in liquid solution.

5.1 Design of the Extraction Setup

The above mentioned studies also show that the ^{131}I daughter ^{131}Xe quickly diffuses out of a liquid iodine solution and dissolves into gaseous state.
For the reasons discussed above, a setup dedicated to the extraction of this xenon must meet the following requirements:

1. Transport xenon gas away from the surface of liquid iodine solution.
2. Eliminate volatile iodine, as well as any other contaminants from the gas.
3. Collect the xenon gas in a suitable container for transport to the gamma-MRI setup.
4. Strictly contain and shield all radioactive material to avoid contamination with ^{131}I or exposure to its radiation.
5. Minimize the time during which manual operation close to the radioactive iodine is necessary.

The last two points are required to meet the strict radioprotection requirements needed when working with high doses of radioactive iodine. Due to the boiling point of xenon at $165.2°K$, the collection of xenon is possible in a cold trap which is cooled to liquid nitrogen temperatures ($77.15°K$).
With these requirements in mind we developed the concept of a *decay loop* as depicted in figure 5.2. A pump should circulate a small volume of nitrogen within a closed loop. On one side of the loop, the nitrogen flows over the surface of radioactive iodine in aqueous solution, thereby picking up any radioactive xenon that has diffused out of the solution. A dedicated filter extracts eventual volatile radioactive iodine before the gas passes a cold trap to collect the radioactive xenon. Since we

are working with an aqueous solution, there is also a possibility of water vapor contaminating the nitrogen atmosphere, which led us to the addition of a purification cold trap filled with dry ice. At $194.65°K$, this should be cold enough to eliminate any water (as well as most other chemical contaminants that we might not have accounted for) from the carrier gas, leading to a purer xenon condensate in the collector trap.

The finalized setup can be seen in figure 5.3. Details on the design and operation of the components are given in the sections below.

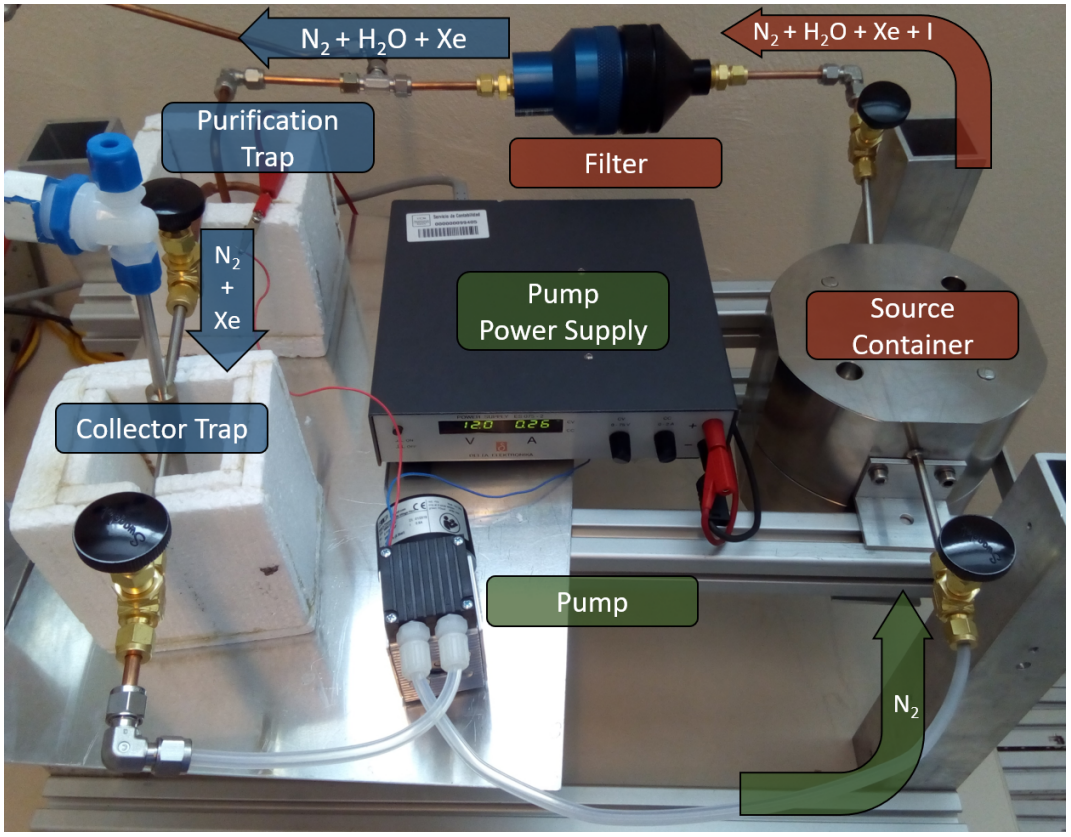

FIGURE 5.3: Foto of the assembled decay setup with component names. The flowing gas mixture is indicated in the arrows. Note that all gases but the nitrogen are only present in trace quantities.

5.1.1 Source Container Design

The most challenging part of the decay loop from a design perspective was the source container for the radioactive iodine. Since large quantities of iodine are required to produce sufficient ^{131m}Xe (1Bq of ^{131m}Xe can be extracted from 3kBq of ^{131}I) , the source container must exhibit a thick layer of shielding. The iodine solution

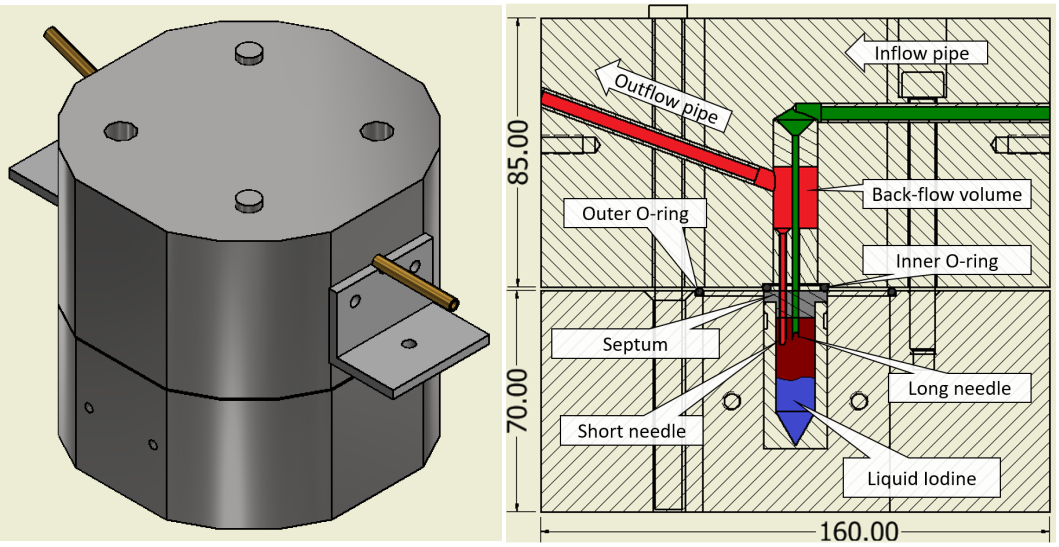

(A) Outside view. (B) Cross-section view.

FIGURE 5.4: Final CAD design of the iodine source container. The clean nitrogen gas (indicated in green) enters through the horizontal pipe followed by the long vertical needle. Once enriched with the radioactive trace gases (indicated in red), it exits through the short needle, the back-flow volume and the slanted pipe. Measurements in mm.

will be delivered in a glass vial with a rubber septum. Due to the high volatility of iodine, opening this vial or even pouring the iodine into another container would immediately contaminate the experimental area to a significant degree. To avoid this, the iodine can only be accessed through a needle that punctures a septum. This is complicated by the fact that in this application a flow past the surface of the radioactive iodine is needed, so that one needle is required for the inflow and another for the outflow of nitrogen. To avoid a direct manual handling of the highly radioactive iodine source, these needles should puncture the septum automatically when closing the shielding of the container. Further, it should be avoided that any liquid escapes the container. Since the inner cross section of the puncturing needles is rather small, even a moderate gas flow can lead to high velocities through the needles, which can lead to a disturbance of the liquid surface and to partial suction of liquid through the outflow needle.

This problem was addressed by an insert for the source container that consists of two steel cylinders, each one holding a hypodermic needle of 2.0 mm diameter and kept at distance by a plastic spacer (see figure 5.5). The long gas-inflow needle, held by the upper cylinder insert, is guided through a hole in the lower cylinder, before puncturing the septum to same depth as the short outflow-needle, which is guided

off-center through the lower cylinder insert. The space between the two inserts serves as a volume where droplets of liquid that are sucked out from the source vial may be collected and eventually flow back into the vial. The inclined exit pipe minimizes the escaping of liquids even further.
The iodine chamber is sealed by two O-rings. The inner one creates a seal directly between the vial and the steel lid and the outer one seals the surfaces of the base and lid steel slabs, establishing a double containment. Figure 5.4 shows the final (of several consecutively improved) designs for the source container.

5.1.2 Membrane Pump Operation

In order to guarantee a fully closed loop, a membrane pump of the model KNF N86KTDC B was purchased for the purpose of gas circulation. After the design of the source container (in particular the choice of puncturing the source vial with needles) was complete, it became clear that a lower flow rate than the nominal 5.5 normal liters per minute (at 24V operation voltage) was desirable, since high gas velocities would increase turbulence in the source vial and therefore the likelihood of liquid iodine being sucked out of the vial.

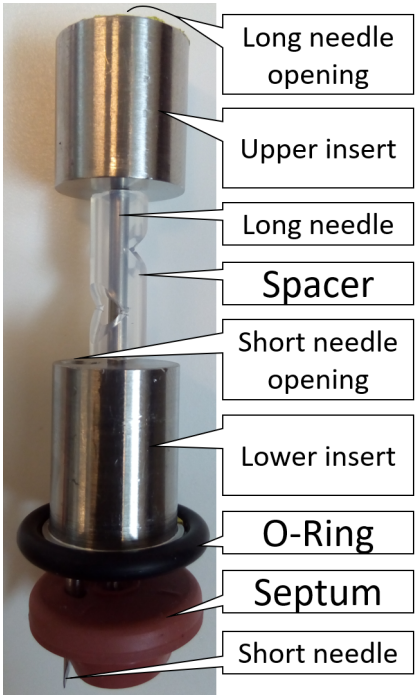

FIGURE 5.5: Manufactured insert for the source container, including the inner O-ring. Needles are still puncturing the septum of the test source vial after a test-run.

According to manufacturer information, the flow rate may be regulated by varying the input voltage of the pumps DC motor up to 30 V, but the expected flow rates for the different voltages are not specified. Tests with a variable power supply showed stable operation of the pump from as low as 8 V[1].

[1]The pump was operating with no or next to no pressure difference between inlet and outlet during these tests.

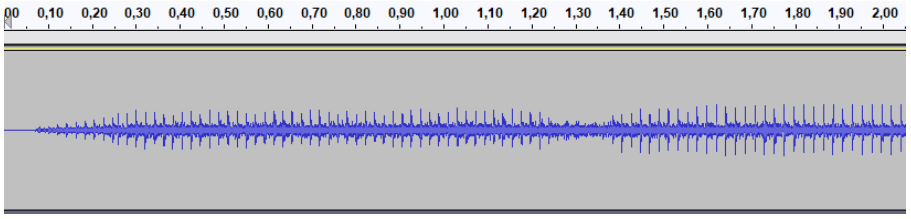

(A) Two seconds of the pumps acoustic signal visualized in an audio editing software.

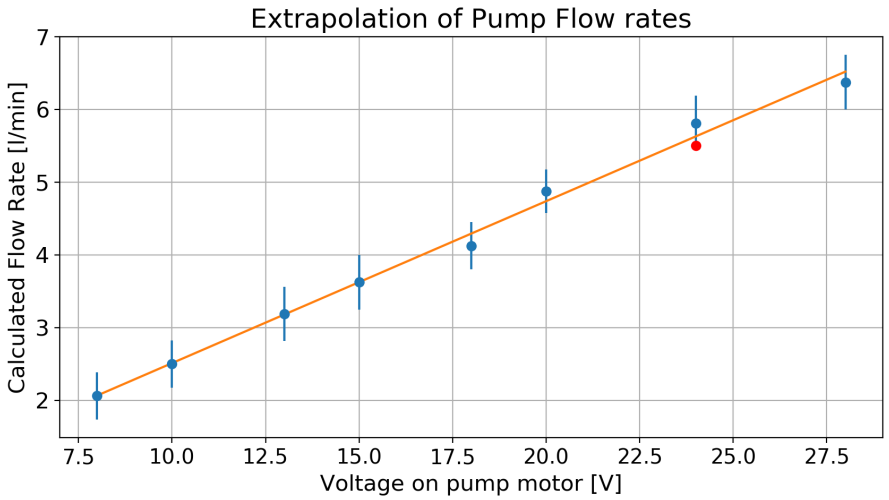

(B) Calculated flow rates generated by the membrane pump. Values are based on the nominal flow rate (red point) and extrapolated based on an acoustic analysis of the motor frequency.

FIGURE 5.6: Calculating the pump flow rate at different operating voltages by acoustically measuring the motor frequency.

Since no direct way to measure the flow rate was readily available, an indirect way was chosen. The motor generates acoustic noise with a frequency proportional to its rotational speed. This noise was analyzed at different operation voltages in an audio editing software by counting the distinct "spikes" in the signal (see figure 5.6a). Analyzing this acoustic "spike frequency" at different voltages revealed a linear relationship of f_{pump} and the voltage U, that could be fitted with $f_{pump}(U) = 1.78\,\text{Hz} + 2.27\,\text{Hz/V}$. Since a membrane pump operates on a simple displacement principle it can be assumed that the generated flow rate is directly proportional to the motor frequency. When assuming that the manufacturers nominal value of 5.5 l/s at 24 V is accurate, we can use this reference value to infer the flow rates at all voltages, leading to the estimates presented in figure 5.6b. Errors were estimated from a constant of 0.25 l/s accounting for inaccuracies during the measurement (error of the power supply, variable pump performance etc.) and a variable error from the spike counting method.

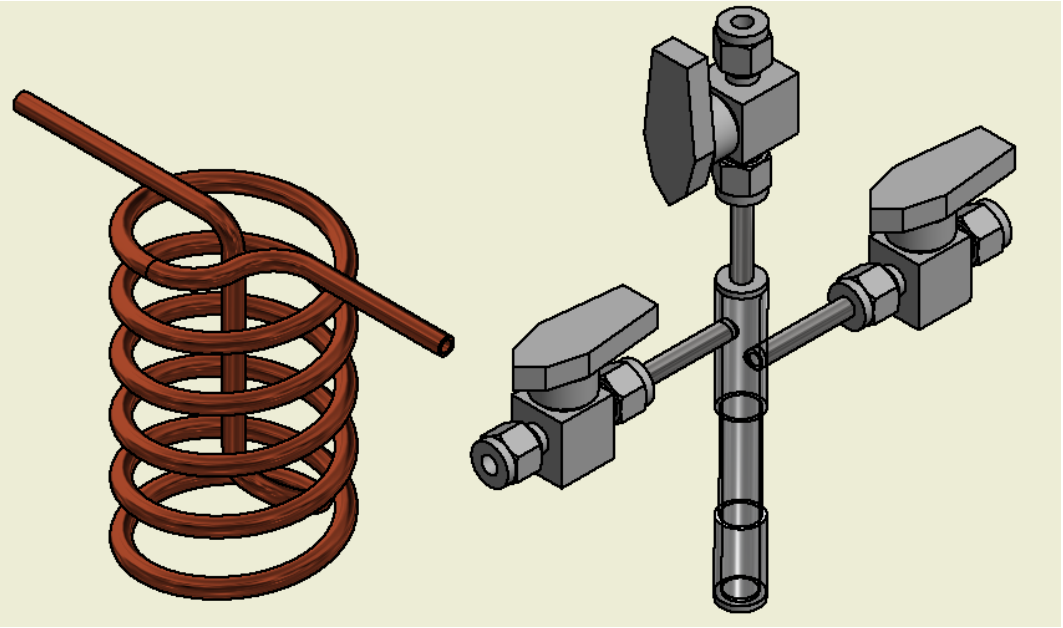

FIGURE 5.7: Design of purification trap (left) and collector trap (right) for the xenon extraction setup.

5.1.3 Cold Traps

Due to security concerns about glass cold traps containing radioactive gas, the cold traps where specially designed from metal and built in house for this setup.
The purification trap does not need a valve for extraction, so a coil design was chosen and produced from a length of 6/4 mm copper pipe[2].
The collector trap also doubles as a transport container for the collected xenon to the gamma-MRI setup. It has a valve for extraction of xenon on the top, so that, once it is connected to the gamma-MRI phantom and tipped on its head, the heavy xenon gas can flow into the phantom assisted by gravity. Inflow and outflow are offset in height in order to promote turbulence and thereby increase the chance of xenon condensing of the walls. The wall thickness in the middle is reduced to 0.75 Hz in order to facilitate gamma-radiation penetrating during operation of the extraction setup. This way, a dosimeter close to the trap can monitor the collection of radioactive xenon. The parts were machined from type 304l stainless steel and laser welded in the CERN mechanical workshop.

[2]The 6/4 mm specification denotes the outer and inner diameter respecively.

5.2 Procedure and Radiation Dose Planning

A radioactive dose suitable for imaging is in the order of magnitude to the 1mCi (37MBq), similar to the one used in [1]. Since only a small fraction (approx. 0.5%) of iodine ever decays to the isomeric state ^{131m}Xe, the required dose of iodine has to be three orders of magnitude higher. Figure 5.8 shows the decay curve of 1Ci

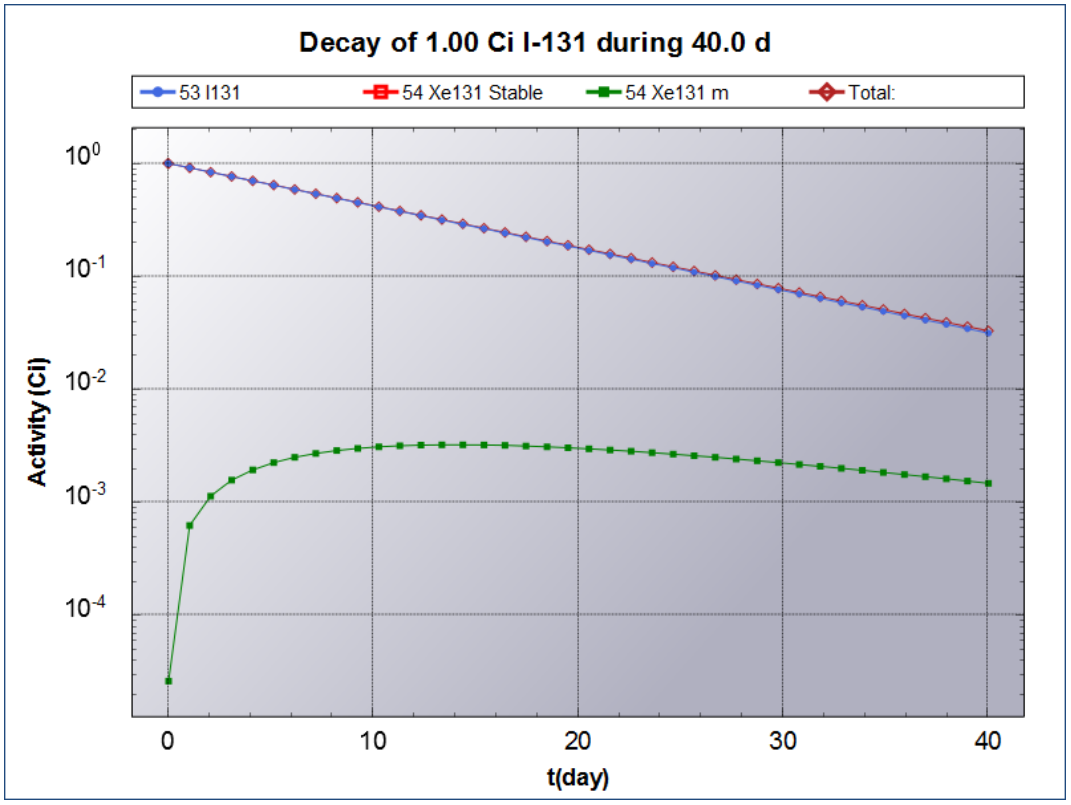

FIGURE 5.8: Decay of 1Ci of $^{131}Iodine$ and the produced quantity of ^{131m}Xe, calculated using the *decay engine* software of Nucleonica.

of iodine. The maximum amount of isomeric xenon that may be extracted from such a source amounts to an activity of less than 3mCi. This means that even if losses[3] can be kept to a minimum, at least 0.5Ci of radioactive iodine need to be handled to generate an imaging dose. This very high dose in combination with the volatile nature of iodine dictates that the extraction of an imaging dose can only be performed in a hot cell. While these exist at the ISOLDE facility, their availability is limited.

For this reason, the plan for initial experiments foresees a significantly lower radiation dose of only 600kBq of isomeric xenon, generated from 5mCi of iodine, which

[3]For example due to xenon not fully dispersing out of the liquid or being caught in the filter.

can be handled under a regular fume hood, as long as a double containment is provided. Double containment in this context means that in addition to the extraction setup itself being leak-tested and situated withing the fume-food, another containment layer must provide an artificial sealed atmosphere around the setup. This is done with a so called "AtmosBag", which is essentially a large plastic bag with gas inlets and integrated gloves, turning it into a flexible glove box. While this dose does not give sufficient statistics to perform imaging experiments (within reasonable measurement times), it does allow to test the performance of the extraction setup, as well as polarization, RF-pulse-sequences and detectors in the MRI setup.
The extraction of this reduced dose was planned and prepared in detail, including the exact dose-planning and risk estimation required for radiation safety approval. The following step list summarizes the extraction procedure:

- Prepare the extraction setup within the AtmosBag in the fume hood. All successively needed tools, as well as the iodine transport container should be in the sealed AtmosBag with the setup.
- Evacuate the extraction setup (valves to the open source container closed), introduce a trace amount of stable xenon[4] and fill the system with nitrogen up to normal pressure.
- Transfer the iodine source vial from the transport container to the source container of the extraction setup and close the source container, puncturing the vial.
- Run the membrane pump until the count-rate in the dosimeter near the collector trap stops increasing.
- Disconnect the collector trap from the extraction setup.
- Exchange gas within the AtmosBag with fresh nitrogen, removing possible gaseous contaminants.
- Open the Atmosbag, secure the remaining setup and prepare the collector trap for transport.

[4]The additional xenon is introduced in order to help the radioactive xenon condense in the cold traps

TABLE 5.1: Results of testing the liquid retainment of the source container with distilled water.

Vol before [ml]	**Vol after** [ml]	**Droplets**
2.00(5)	2.00(5)	No droplets found
2.85(5)	2.45(5)	Droplets found in between inserts
4.00(5)	3.10(5)	Droplets found in piping up to the pipe before the filter. None in the filter holder.

The risk estimation for the extraction procedure can be found in appendix D.

5.2.1 Liquid Retainment Tests

Using a test vial filled with distilled water, the retaining of liquid in the source container was tested. For this, the system was operated in air at normal pressure for five minutes at a pump voltage of 12V. Before each test, the vial was filled with a known amount of distilled water. Afterwards, the remaining amount of water in the vial was measured using a pipette and the piping between the source container and the filter was disassembled and visually checked for liquid droplets on the walls. For these testing purposes, a carbon filter was used instead of a silver ceolite filter, which should generate the same pressure drop. The results of the test are shown in table 5.1.

Based on these results, operating the setup with no more than 2ml of liquid iodine in the vial appears ideal. This corresponds to the vial being filled to about half its height. The tests with 4ml have shown a noticeable deposition of droplets in the piping walls, which is listed as a low-severity incident in the risk estimation plan for the procedure (see appendix D), leading to a dose-rate of up to 31 μSv for the operators of the fume-hood. Operating the setup with 2-3ml seems to be uncritical thanks to the flow-back designs discussed in section 5.1.1, but since no advantage is to be gained from increasing the amount of liquid (other than the limitations on iodine concentration given by the iodine delivering company), this limit should not be pushed.

Chapter 6

The gamma-MRI Setup

For an initial setup, we chose to utilize existing MRI components which were for the most part made available by the the group of Jean-Noël Hyacinthe at HESGE. Between 12.-16.03.2018, the setup was first assembled at HESGE and core functionalities were established and tested. Figure 6.1 shows an overview of the central components, which are discussed in more detail in this chapter.

6.1 Measurement and Polarization Position

In principle, gamma-MRI measurements can be performed even at the same time and place as the SEOP pumping is performed, without even moving the target vial or the polarized xenon therein. However, in any real imaging application, this will not be the case, since the xenon can not be hyper-polarized e.g. in the lungs of a patient. Therefore, the SEOP and the gamma-MRI will always have to be performed in separate locations. This is one reason why we chose to mount the target vial on rails, enabling it to move between the optical pumping and measurement positions. The second reason is the confinement between the magnet poles, which are only 154 mm apart. The optical pumping must be performed in such a way that the circularly polarized laser beam is parallel to the magnetic field direction when it is absorbed by the rubidium. It was desirable to use the available target vial (see figure 6.2b), which was produced for previous work [10] and is optimized to reach good polarizations. It is also conveniently designed as two concentric cylinders: the

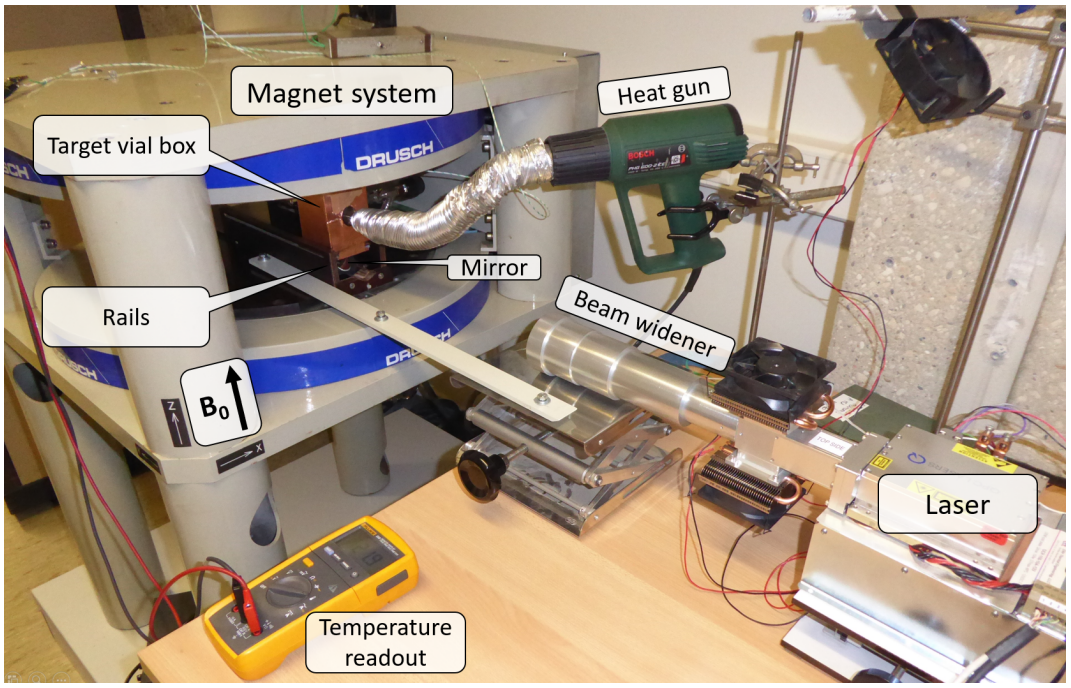

FIGURE 6.1: Overview photo of our gamma-MRI setup. Visible on the right is the diode laser for SEOP pumping, mounted on a cooling unit. It is directly coupled to a beam widener which appears on the picture as a incrementally widening aluminum tube. The laser beam is reflected upwards by a mirror under the target vial, which is later moved to its polarization position within the MRI magnet system. A conventional heat gun blows hot air through an aluminum hose on the target vial in order to heat it to the required temperature. A multimeter connected to a PT100 temperature sensor measures the temperature of the target vial. The detectors around the measuring position are not visible in this picture, since they are located in the center of the magnet.

inner one contains the rubidium and xenon that will be optically pumped and the outer one acts as an oven when hot air is blown through it. Fitting the system between the magnet poles was very challenging. The design as presented in figure 6.2 was made possible by slim detector design and a custom 3d-printed holder for the mirror[1].

As a material for the rail system and the structural parts holding the target vial, we chose a resin-reinforced plywood (Lignostone®Transformerwood®), which is produced for the casings of electrical power transformers. This material is machinable, harder than most plastics, non-magnetic, non-conductive and is rated to permanently withstand high temperatures of $100°C$ (and higher temperatures for short durations) without deforming.

The target vial itself was fitted between two pieces of this plywood, which were

[1]Commercially available mirror holders would not fit into this confined space.

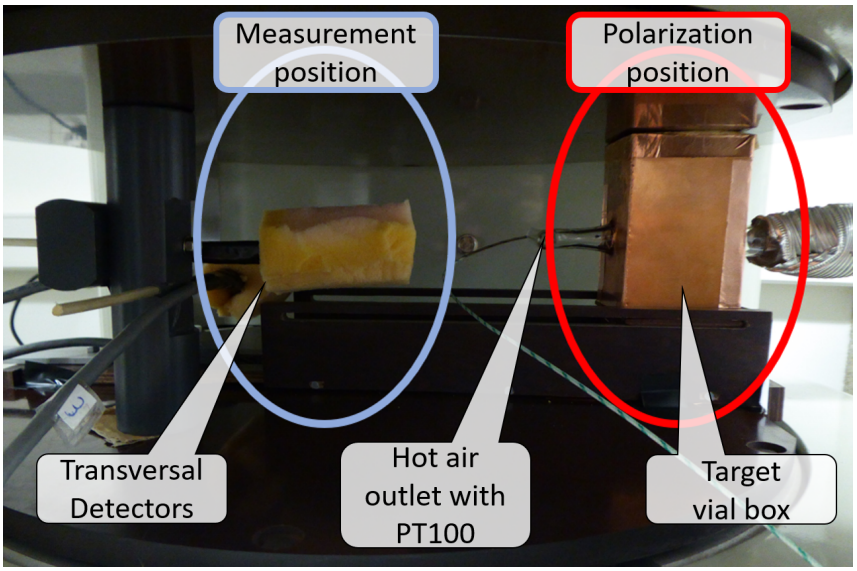

(A) The photo shows the system in polarization position with the hot air tube connected, as well as the transversal detectors and the cable of the PT100 temperature sensor measuring the hot air exiting the target vial.

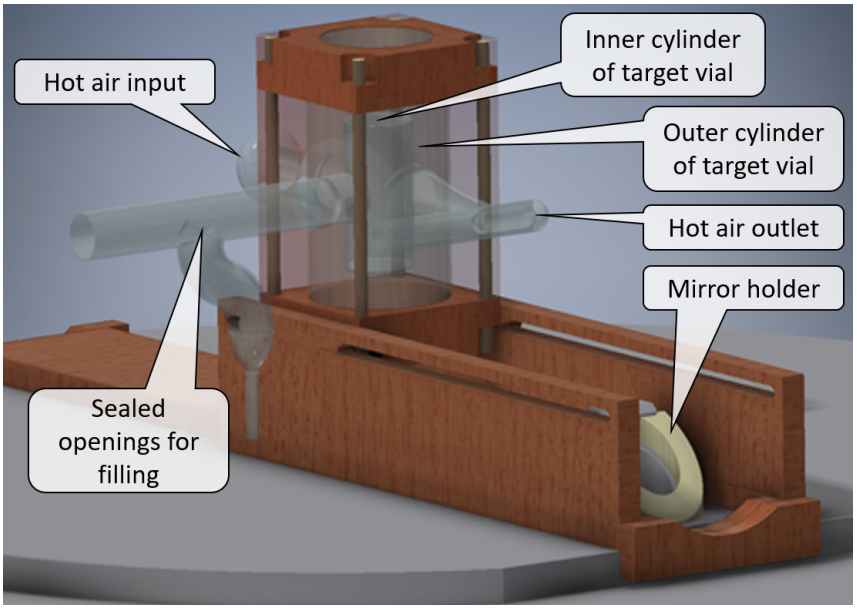

(B) CAD-drawing, showing the box in "measuring position". The copper casing of the target vial box is set to transparent to show the inner design. The holder for the laser mirror is visible on the right.

FIGURE 6.2: Photo (A) and CAD-drawing (B) of the setup between the magnet poles, including the rail-system, mirror holder, the target vial and the box holding it.

machined to an exact fit[2] around the glass (process shown in figure 6.3a) and held

[2]Two nearly identical glass vials were available, one of which had shown slightly higher polarization values in the past ([10]). Since this "good" vial was not to be risked by taking it to the workshop, the clasps were designed to fit the other one. Unfortunately it turned out later that the "good" vial has slightly smaller dimensions, so that some glass-fiber wool was necessary as a buffer to create a good fit of that vial between the clasps.

together by four polyester rods. To act both as a layer of insulation as well as a Faraday shield between RF-coil and detectors, a cage of 200μm copper sheet was placed around the target vial. The bottom of the cage has a 3cm hole to permit the laser beam and the top plate was coated with graphite paint on the inside to absorb the laser radiation. The finished target vial box is shown in figure 6.3b.

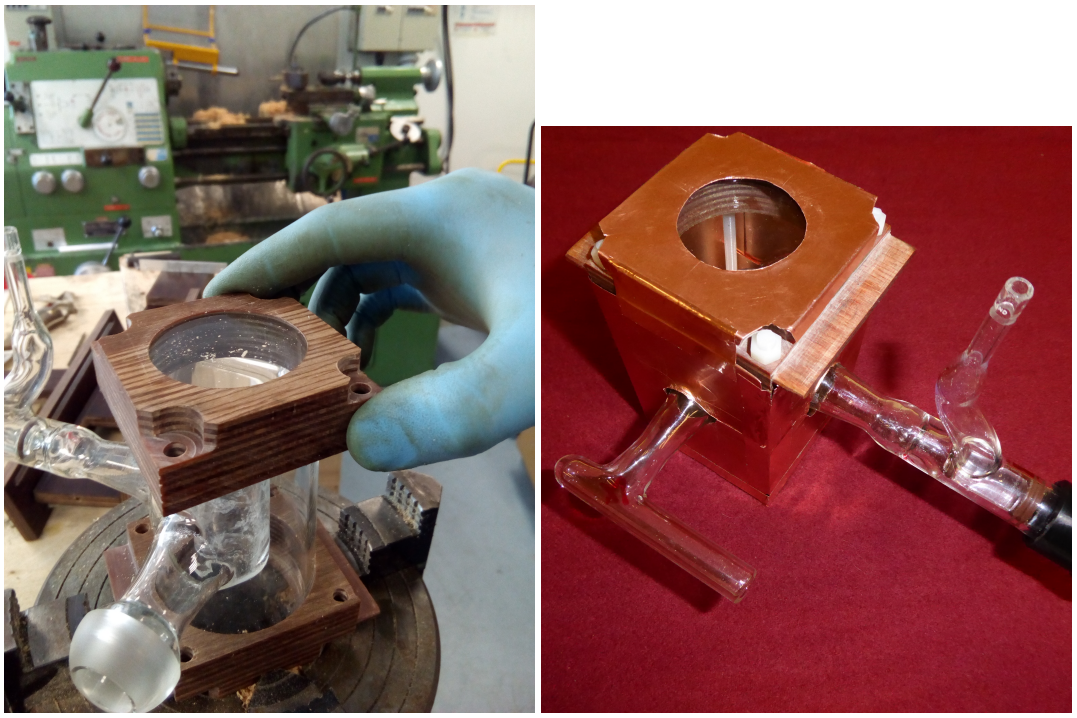

(A) Target vial chamber during manufacturing.

(B) Target vial in completed box.

FIGURE 6.3: Target vial box during and after manufacturing.

The rail system can be clamped onto the lower magnet pole. A fan was mounted to one end of the rail system (see figure 6.4) to prevent a build-up of hot air between the magnet poles and to provide a cool air flow for the temperature-sensitive gamma-detectors. The fans distance to the rails later had to be increased, since the magnetic field was interfering with the electric motor of the fan.
Figure 6.5 shows the final assembly of the rail system with detectors and target vial chamber (in polarization position) installed between the magnet poles.

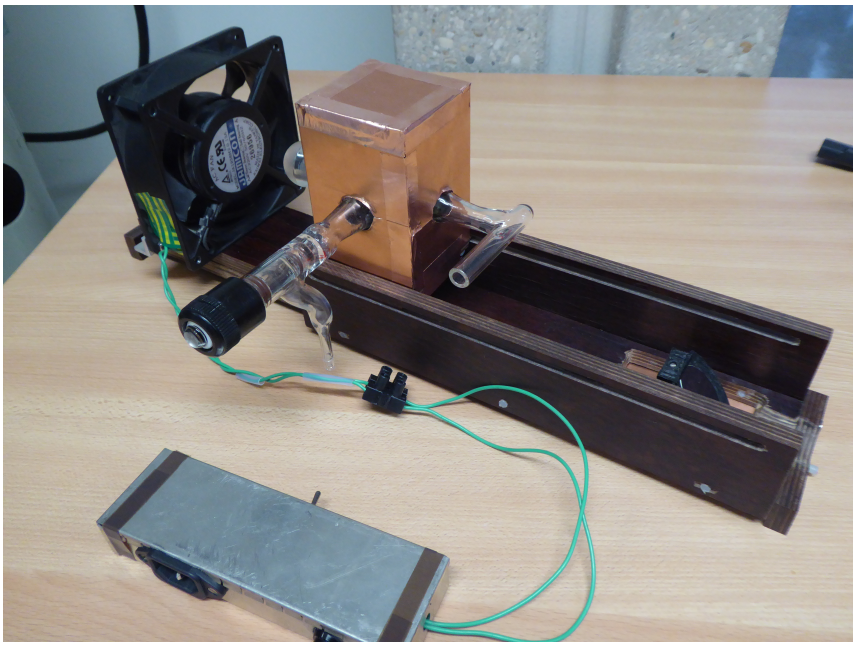

FIGURE 6.4: Rail system with mounted target vial chamber, mirror and cooling fan after its initial assembly in the workshop.

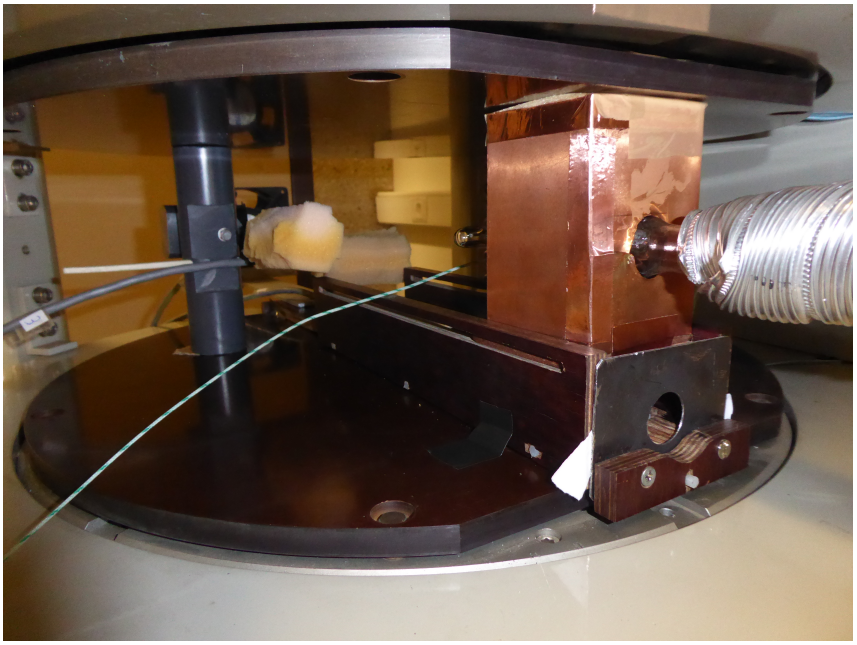

FIGURE 6.5: Complete rail system, detectors and target vial chamber in polarization position within the magnet.

6.2 Magnet System

We chose to use a 0.1T low-field MRI system based on an open, water-cooled resistive magnet made by Drusch (Poissy, France), available in the laboratory of Jean-Noël Hyacinthe. The system provides enough space between the poles and has a large area of high magnetic field homogeneity suitable for imaging purposes. Shimming and gradient coils are integrated into the magnet poles. The homogeneous area is rated to $\pm 5ppm$ within a central volume of 10×10 cm^2 in the horizontal and 6cm in the vertical direction.

The homogeneity before shimming was also measured during the hardware-tests using a Metrolab precision teslameter. The NMR-probe of the teslameter was fixed to a wooden base and shifted in 1cm steps along the respective axis and the measured field strength was tabulated. Figure 6.6 shows the spatial deviation of the central field value in ppm. The field in the middle of the magnet was measured at 0.101054 T when scanning the x-axis, while the center of the y-axis was at 0.100852 T. These values directly contradict each other, since the axes cross at this location and should therefore exhibit the same magnetic field strength in this location. However, the teslameter is rated to a 0.1 μT precision and shifting the probe back to reproduce previously measured values at several positions yielded values deviating less than 1 μT from the previously measured ones. For this reason we exclude temporal drifts in the magnetic field as a possible reason. One consistent difference was that for the x-axis measurements, the probe was inserted from the side, while it was inserted from the front for the y-axis measurements. However, even if the probe ended up in a slightly different angle during both measurements rows, only the intensity of the NMR signal but not its position, i.e. the measured field strength should be affected. Clarifying the error in this measurement will require a repeated measurement, which will be necessary in any case once the shimming is activated and correctly calibrated. Because measurements could be reproduced on each axis, we can assume that the relative precision of the measurement is good. With this assumption, we can report a homogeneity of better than 60 ppm along the x axis and better than 40ppm along the y axis. This measurement shows that the unshimmed field is one order of magnitude worse compared to the specifications for a shimmed system, which should be within capabilities of the shimming system to compensate.

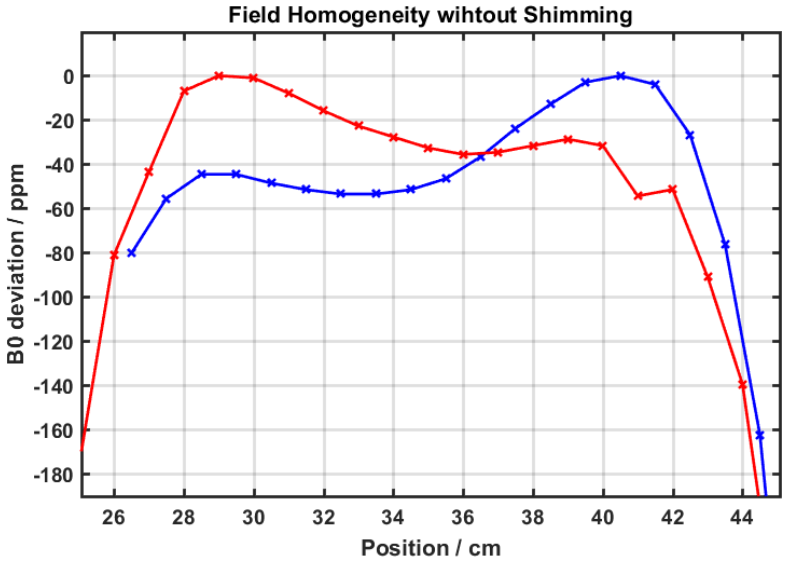

FIGURE 6.6: Measured magnet field homogoneity in the central x (blue) and y (red) axis. The central value of the x-axis was measured at $1.001054T$, while the center of the y-axis was at $1.000852T$

6.3 Laser System

The laser light for the polarization is provided by a laser diode array with an *integrated volume holographic grating*; the model is called BrightLase®Ultra-100^{TM} from QPC Lasers (by Laser Operations LCC, Sylmar, CA) and provides a 50 W continuous-wave $794.7 \pm (0.3)$ nm beam with 0.4 nm maximum spectral bandwidth, coupled to an 800 μm optical fiber. After leaving the fiber, the beam is widened by a custom beam expander telescope (also provided by QPC) to a diameter of 25 mm and passes a quarter-wave plate to generate circular polarization. Directly under the optical cell (moved into polarization position), the parallel beam is reflected by 90 degrees, hitting the entire volume of the SEOP gas mixture unfocused for maximum absorption. To achieve a good preservation of circular polarization, we chose an elliptical silver coated mirror with a nominal reflectance of better than 96% at this wavelength.

Figure 6.7 shows the target vial irradiated by the laser, as it will be during spin-exchange optical pumping. A smartphone-camera was used for alignment purposes, since its lack of a good infrared-filter allows it to show the intense, but normally invisible, near-infrared laser light.

A circular aperture attached to the rail system was added after the imperfectly

aligned laser-beam had exceeded the limits of the elliptical mirror and damaged (partly melted) the mirror holder, which is 3d-printed from Acrylonitrile Butadiene Styrene (ABS).

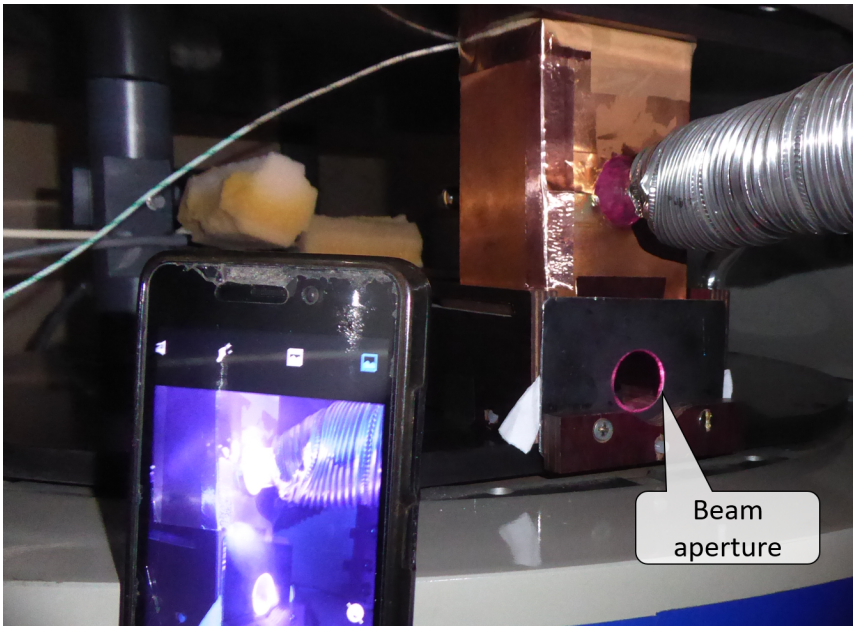

FIGURE 6.7: Photo of the chamber during laser operation. The infrared radiation appears as a weak purple in the main photo, but as a bright blue-white on the smartphone camera.

6.3.1 Heat Development during Laser Operation

An initial worry was that the heat from 50W of laser light hitting the top copper plate of the target vial chamber, in connection with the hot air, could damage the polymer cover of the upper magnet pole, which is in direct contact to the target vial chamber. Therefore, the temperature was measured alternately at the hot air outlet of the target vial and in between the top magnet pole and the target vial chamber (which is additionally insulated with a thin layer of glass fiber wool). At the same time, both the laser and the heat gun were operated at various power settings.
Operating only the heat gun at its maximum setting (rated to $600°C$) resulted in the copper tape of the target vial loosening, but the temperature at the magnet pole did not exceed $72°C$[3]. Operating only the laser at maximum power heated the top

[3]This and the following temperatures were measured with the PT-100 temperature probe. Due to the fluctuations during the measurements we estimate an error of up to $\pm 5°C$.

plate to slightly over $55°C$.
As a suitable setting for SEOP, the heat-gun was set to power level 5, corresponding to a nozzle temperature of $158°C$. This resulted in a temperature of $95°C$ at the air outlet of the target vial and $60°C$ at the magnet pole.
When adding the laser on maximum power, the temperature at the magnet pole rose close to $90°C$ while the temperature at the air outlet did not change significantly. Afterwards, no damage was found on either the target vial or the magnet pole.

6.4 Detectors

Most commonly, gamma detectors are built by connecting a photomultiplier-tube (PMT) to a scintillator crystal. An incoming gamma-photon interacts with the scintillator material, thereby generating many photons of lower energy. These in turn generate electrons in the photocathode of the PMT, where they trigger an electron cascade that is detected as an electronic signal. Provided that the gamma-ray was fully stopped in the scintillator material, the number of generated secondary photons, and therefore the magnitude of the final electronic signal, is proportional to energy of the original gamma-ray.
For this experiment however, the gamma-detectors need to be situated inside a magnetic field, which is strong enough to disturb the paths of electrons within the PMT, thereby compromising its proper function.
In the PNI setup presented by Zheng et al. [1], this problem was circumvented by adding long light-guides between the scintillators and the PMTs, so that the latter could be situated outside of the magnetic field.
However, such light-guides generally lead to a relatively bulky design and would likely need to be custom-made.
We have therefore opted for the more state-of-the-art alternative to PMTs, namely silicone photomultipliers (SiPM). These consist of arrays of avalanche photodiodes (APD) and can fulfill the same role as a photomultiplier tube. But, since the electron-avalanche is spatially confined to a silicone layer of only micrometers of thickness, it should not be significantly disturbed by the presence of a magnetic field. Another advantage is the very small size of these diodes. Gamma detectors

with SiPMs are already widely used, especially in PET devices.
This reasoning lead us to the collaboration with the group of Luis Fraile and Jose Manuel Udias Moinelo from the Complutense University of Madrid. Their students, Victor Sánchez-Tembleque Verbo and Miguel Garcia have put together suitable gamma detectors and designed simple electronic boards for this project using small (8.6x8.6x30mm) NaI-Scintillitors with SiPMs of the model Hamatsu S13360-6075CS. As opposed to the common designs known from PET-detectors, the SiPM is not directly attached to a circuit board with the electronic circuit that drives the photodiodes, but a via a cable, which allows the electronics to operate outside the magnetic field.

6.4.1 Detector Support Structure

To mount the gamma detectors realized by Sánchez-Tembleque Verbo and Miguel Garcia in the setup, a support structure with two detectors in transversal positions and one in a longitudinal position was built. It needed to be rigid enough during a measurement, but could not be glued or screwed to the magnet pole, since the MRI system is also needed for other experiments. The detectors further need some space around them for insulation, as well as a cooling air flow around said insulation, which was provided by a fan from outside the magnet. Further, it needed to be constructed from non-magnetic materials, as it would otherwise disturb the magnetic field homogeneity.
A support structure was machined from PVC. The detectors were mounted on slightly tapered wooden rods of 5mm diameter, which tightly fit into corresponding holes in the PVC structure. The longitudinal detector was mounted into a pocket in the bottom plate of the rail system (see top part of figure 6.8a). The transversal detectors were fixed to a PVC rod that is clamped tightly between the magnet poles. This support system works very satisfactory, with the possible drawback is that the relative position between the target vial and the detectors cannot be defined accurately, since all parts move individually. However, since a baseline asymmetry is subtracted from all gamma-MRI measurements in any case, this is not problematic for the measurement as long as the parts are not moved with respect to each other between baseline acquisition and measurement.

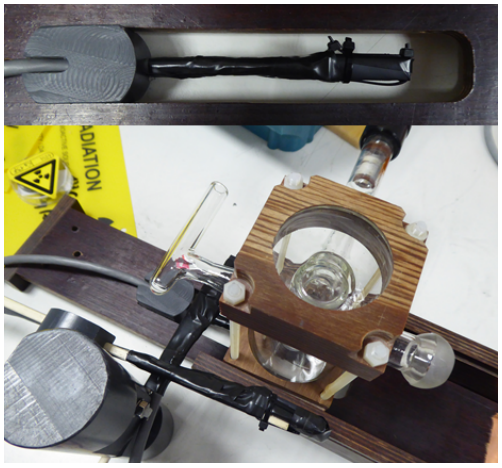

(A) Rail system and detector support without insulation. The detailed view on top shows the longitudinal detector in its pocket within the rail system's bottom plate.

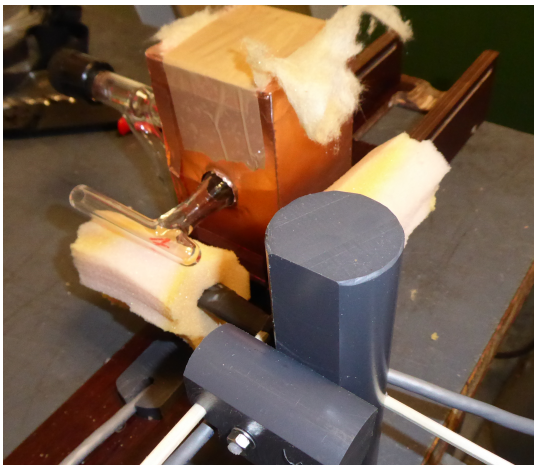

(B) Rail system an detector support structure with insulation.

FIGURE 6.8: Rail system in measurement position and detectors, both with and without insulation, set up outside the magnet to allow a clear view.

6.4.2 Gamma-Detectors in the Magnetic Field

In order to make sure that the gamma detectors and their electronics are in no way compromised by the magnetic field, the circuit boards in our setup are situated outside of the magnet and are connected to the SiPMs with cables. A measurement (see figure 6.9) using a ^{152}Eu source[4] was performed to analyze the detector performance inside and outside of a magnetic field.

The spectra (figure 6.9a) show clearly that the overall magnitude of the peaks inside and outside the magnetic field are in good agreement. In a closer analysis (figure 6.9b), we compared the differences between the counts in each energy bin with and without magnetic field to each other and to the statistical error. In combination, the plots show that the peaks recorded inside a magnetic field exhibit a systematic shift towards the lower energies compared to the peaks recorded without magnetic field. The effect becomes more prominent in the high-energy regime. This shift is similar to the one expected from a change in the energy-calibration of the detectors. The effect is however not large enough to be problematic for the gamma-MRI experiment and could even be easily corrected by calibrating the detectors to the xenon

[4]This isotope was chosen because it has two gamma-lines at 121keV and 244 keV, which allows to interpolate the detector behavior for the 164keV xenon-line that is of interest.

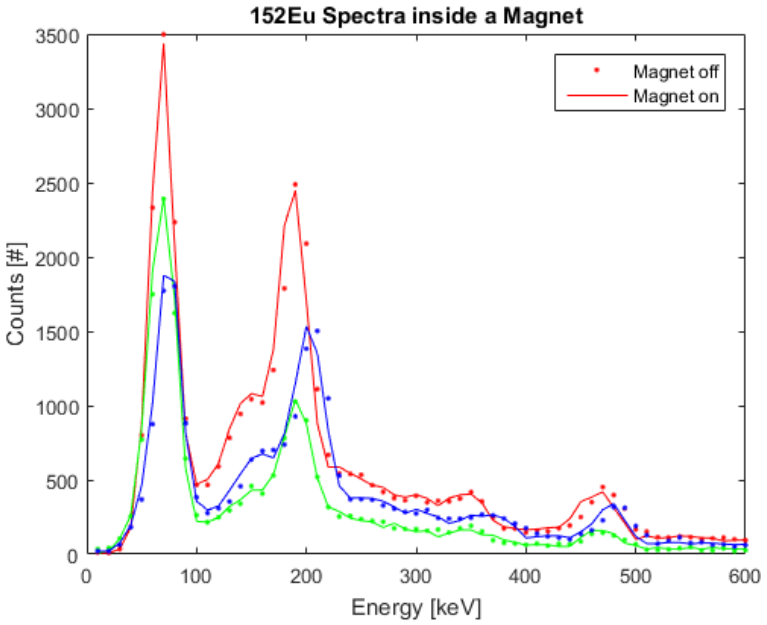

(A) Spectra of all three detectors, each plotted in one color (red, green and blue) using lines and dots, representing a measurement within and without the magnetic field, respectively.

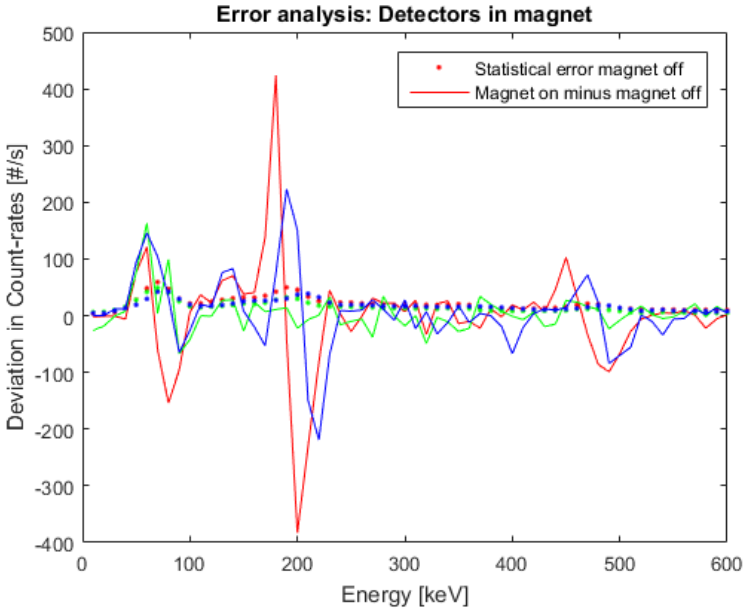

(B) Comparing the differences of the magnet on and magnet off spectra to the statistical error reveals a shift in the energy calibration.

FIGURE 6.9: Analysis of the detector test data. Source and detectors were fixed in position, while only the magnet was switched on and off between measurements.

spectrum within the magnetic field.

6.4.3 Temperature Stability of gamma Detectors

The electron avalanche effect of APDs as those used in our detectors strongly depends on the temperature [19] of diode operation. For example, the Hamamatsu detectors we use are rated to have a temperature dependent operating voltage of $3V + 54mV/°C$. If the temperature of the detectors would change during a measurement, it would therefore affect the effective operating voltage and in turn the sensitivity and the measured count-rate.

To avoid a significant temperature effect on the count-rates, we aimed at a maximum temperature deviation of $0.5°C$ during the measurement[5].

Meeting this requirement was somewhat challenging, since during a gamma-MRI experiment, the target vial needs to be heated to $100°C$ for the SEOP process and immediately afterwards shifted to the measurement position, where the distance between the target vial's outer wall and the detectors is less than 2 cm. This problem motivated the use of acopper cage[6] around the target vial as well as the foam insulation around the detectors. Additionally, a fan was added to provide a cooling air-flow past the detectors.

The temperature stability at the detector locations in our test setup was measured after the heat stability tests described in section 6.3.1. The target vial was first heated by hot air and the laser, tuned to full power as it would be during the SEOP-process, and immediately afterwards moved to the measurement position. During the whole process, the temperature was measured inside the insulation of the bottom detector, which is the closest to the vial[7]. We observed a rise in temperature from $25.0°C$ to $25.3°C$, which is within the desired limit of $0.5°C$.

6.5 Detector Simulation

The expected efficiency of the NaI scintillators was simulated with the *Gamma Spectrum Simulator Pro++* webtool offered by *Nucleonica*. The simulation included no filters or covers of the detector, but the tape around the crystals was simulated as a

[5] Value recommended by Luis Fraile for the detectors designed by his group.

[6] The other motivation for the copper cage is to shield the detectors from RF noise of the RF coil, as well as the RF coil from possible electronic noise from the detectors.

[7] The bottom of the vial is bare of copper since it needs to permit the pumping laser. Keep in mind the difference in emissivity of glass ($\epsilon \simeq 0.92$) and oxidized copper ($\epsilon \simeq 0.65$)

0.5mm layer of polyethylene. The simulated geometry had a circular NaI scintillator with 30mm radius[8] and 8mm thickness, 50mm away from a point-source of 1MBq of ^{131m}Xe.

In the energy window between 100keV and 200keV, the simulation generates an

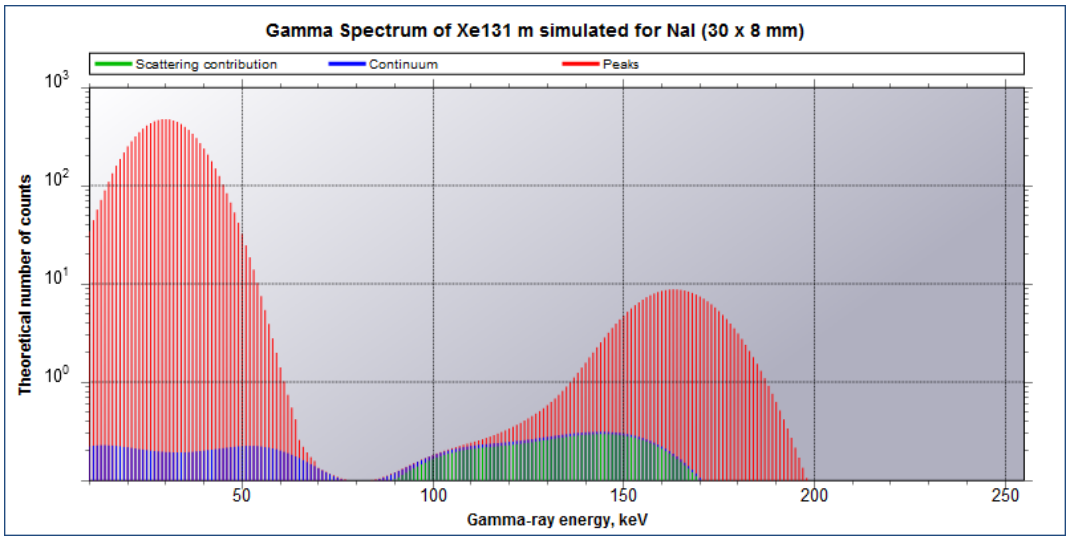

FIGURE 6.10: Simulated Spectrum of 1MBq ^{131mXe} in 5cm distance to a NaI detector.

average total of 276 counts per second. Since no other emission lines contribute in this area and the background is negligible, all of these counts likely come from the 164keV emission line of interest. For the 1MBq source, we expect 19800 of these photons in average per second. Multiplying with the solid angle, we expect 423 of these photons to reach the detector. Based on this calculation, we derive a detection probability of 65.2%.

To verify these simulations, we also measured the count-rates generated by a ^{137}Cs source of 39.9kBq at a distance of 5cm from the detector, obtaining 55 ± 3 counts per second. A simulation analogous to the one above predicts 170 counts per second for a round detector of 30mm radius. Accounting for the three times larger detection surface, we arrive at an expectation of about 57.8 photons per second, which is in very good agreement to the observed value.

[8]The crystals used in reality are also 8mm thick, but have a rectangular sufrace of $8mm \times 30mm$. Unfortunately, the tool cannot represent this geometry. At a constant scintillator thickness, I expect the detection probability per solid angle to be mostly independent from the detector area.

6.6 RF System

The setup uses a custom self-made RF-architecture from the group of Jean-Noël Hyacinthe which has all typical components of a regular MRI setup. In principle, one could implement a much simpler architecture for this experiment, since no RF-reception is necessary for the main experiment. However, the ability to perform regular proton MRI as well as hyper-polarized MRI on stable xenon gives a valuable reference to the measurements: It allows the comparison of images taken with the different types of MRI, but recorded with the same setup. Since the method of regular and even HP-MRI is well established, this approach should also make it easier to find and characterize flaws in parts of the setup when measurements do not succeed on a first attempt.

The downside is that the full RF system must be able to work at the Larmor frequencies of protons (4.272 MHz), ^{129}Xe (1.190 MHz) and ^{131m}Xe (138.2 kHz), which did turn out to be a significant challenge.

The schematic of the architecture is shown in figure 6.11. The development of this system is done by Jean-Noël and his team and the system is functionally equivalent to those found in the pertinent literature on MRI systems (e.g. [3]). As is visualized in figure 6.11, the system is designed around a Radio-Processor-G^{TM} PCI card from the company SpinCore^{TM} (Gainesville, Florida), which incorporates the conversion between analog and digital signals as well pulse modulation and phase control components. The only additionally required components are the respective RF amplifiers and a *duplexer*, which is an electronic component that ensures that none of the strong electronic signal from the *RF-pulse power amplifier* interferes with the weak induction signal from the sample. During the test-phase in March 2018, the RF system was tested on proton and stable xenon samples, which showed that further the control program and some of the homebuilt electronics needed further modifications to allow good signals at all three desired frequencies. These adaptations are still being finalized by Jean-Noël Hyacinthe and his team.

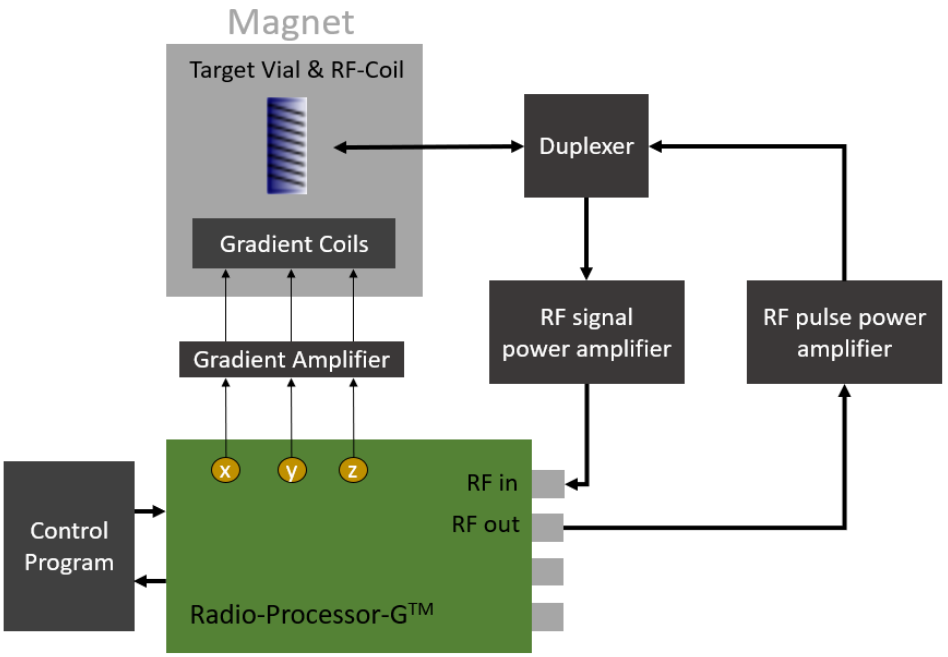

FIGURE 6.11: Simplified scheme of the RF architecture for the gamma-MRI setup.

Chapter 7

Conclusion and Outlook

When this thesis was first planned, the project outline read "Preparatory phase of decay studies using NMR/MRI with laser spin-polarized radio-nuclei, with resonances detected via asymmetry in emission of gamma rays, following ref [1]: [...]". Looking back at the work done in the last eleven months, this has been achieved. The "preparatory phase" was expanded to the point where two separate experimental setups were fully developed, built and tested. The developed simulation software can accurately predict the spin behavior in a gamma-MRI type measurement (demonstrated in appendix A). It was therefore used to prepare the measurements suggested in this work. Unfortunately due to the time constraints on this work, the correct sampling of the k-space and consecutive image reconstruction was not yet successful. Once this has been corrected, the simulation software can also be used to predict imaging experiments and help in the development and testing of new imaging algorithms.

A decay setup for the extraction of ^{131m}Xe from commercially available ^{131}I was developed, built and tested. This provides the project with a source of the required radioactive tracer, unimpeded by beamtime schedules and the upcoming ISOLDE shutdown.

Finally, a first gamma-MRI setup was designed and built. It required us to bring together proficiencies from the fields of radiation from aligned nuclei, spin-exchange optical pumping, gamma-detector technology and nuclear magnetic resonance spectroscopy and imaging. The result is a fully functional prototype setup, assembled

mostly from relatively standard parts, which also bodes well for the cost-efficiency of future designs.
In this light, I am happy to report that upon the writing of this thesis, the project is, in all aspects on which I have been working, ready for its first measurements.
Nevertheless, this project, as well as gamma-MRI as an imaging modality, is still in its infancy. In the next lines I will lay out my view on the future of both.

7.1 The next Steps with the present Setups

As soon as the modifications to the RF-system are complete, the gamma-MRI setup needs to be tested by performing a basic NMR and MRI measurement, first on protons and then on hyper-polarized stable xenon. These tests will also be used to perform the magnetic field shimming and to commission the spin-exchange optical pumping process inside the 0.1T magnet.
Once this is successful, a first 5mCi dose of radioactive ^{131}I in liquid solution will be ordered from Polatom®, and the decay setup can be commissioned in a fume hood, following the detailed plan described in section 5.2 and appendix D. The resulting dose (up to 600kBq) of ^{131m}Xe will then be transported to the laboratory at HESGE and transferred to the target cell.
With this small dose, non-imaging experiments will be performed smiliar to those termed "Polarized Nuclear Detection" in [1]. They will include measuring the degree of polarization by regular HP-MR and via the degree of gamma-anisotropy, thus comparing the two methods.
Without any additional effort, recording the decay of this gamma-anisotropy will also reveal the T_1 relaxation time.
Next, the RF-pulse durations for 90° and 180° pulses on ^{131m}Xe nuclei will be determined experimentally.
It might also be interesting to map out the angular distribution of gamma-rays by turning the magnetization of xenon nuclei to different angles with respect to the detectors using small-angle RF-pulses. By comparing this measurement with results from the anisotropy tool (see section 4.1), information about the m-state distribution after the hyper-polarization may be inferred.

It should also be possible to make measurements of the T_2^* and T_2 relaxation times in a way similar to that reported in [20] and [21], with the difference that gamma radiation instead of beta particles would be detected.
In principle, it is also possible to observe Larmor-precession directly as an oscillation in the detector count-rates (which would effectively result in an FID-measurement). In the same way, Rabi-oscillations can be directly observed during continuous RF-application. Both of these measurements have been reported in [1] with a very similar setup. However, recording such a signal would require a coherent summation over many polarization cycles; that is only possible with a precise time-stamping of the gamma-count events from the detectors, which is currently not implemented. Even then, considering that [1] used a higher activity (leading to a stronger signal) and a much lower magnetic field (leading to slower oscillations), this measurement would be challenging.

A very useful extension to the simulation software would be the introduction of statistical errors. The simulation calculates count-rates directly as a product of partial emission and absorption probabilities, solid angles and number of radiating decays. Therefore, statistical errors due to the quantum nature of the radiation are not reproduced. However, a statistical error could be included by adding an activity-dependent error to the intensity of each `ray`. This way, the simulation could also be used to make accurate predictions about the signal-to-noise ratios in measurements with different resolutions and radioactive doses.

Once the above measurements have been performed, one may acquire and use to a larger xenon dose, suitable to acquire images. Likely, this dose will be in the range of tens of MBq of radioactive xenon. This dose may also be extracted from iodine using the decay setup, since the decay setup was designed with this activity in mind. However, since the required dose of ^{131}I would be in the order of 0.5Ci, radiation protection rules then require the extraction to take place within a hot cell.
Before this experiment, I recommend using the simulation program described in chapter 4.2 and feed it with the values of pulse durations and relaxation times measured in the previous measurements, in order to simulate the required radiation dose

and imaging gradients as well as to test the imaging algorithm. This will necessitate completing the image reconstruction part of the simulation program, but should prove very useful both in preparing and evaluating the experiment.
Using the concept of incrementally increased complexity, it might be desirable to start with a two-dimensional projection image, and proceed afterwards to initially low-resolution 3d-images. Further, an image of the current target vial, having the shape of a simple cylinder with a pipe leading to it, would be relatively uninteresting in its structure, so a custom made target vial with a more intricate shape could be desirable to demonstrate imaging. As a simpler alternative, a transparent gas-displacing object could be inserted into the current vial, which would show up as a negative shape in the image.

At any point during this development, a gamma-MRI measurement can also be performed on ^{133m}Xe, which has very similar properties to ^{131m}Xe, as the isomer also has a long-lived isomeric state (2.19d for ^{133m}Xe compared to 11.84d) with a spin of $I = 11/2-$, decaying to an $I = 3/2+$ ground state; but it exhibits a better branching ratio of gamma-emission (10% compared to 1.91%). For an application, this would mean that ^{133m}Xe would provide five times more statistics for the same imaging dose, which would also decay six times faster, which makes the medical administration to patients less problematic. It will therefore be interesting to demonstrate that these favorable attributes can be utilized in a gamma-MRI measurement.
^{133m}Xe cannot be extracted from radioactive decay of an isotope so readily available as ^{131}I. For this reason, a letter of intent [22] for the collection of ^{133m}Xe at ISOLDE has already been submitted and granted.

7.2 Gamma-MRI on the Horizon

At the current stage it is difficult to say if gamma-MRI has the potential to be the basis of a new widely used commercial imaging modality. Its enormous strength lies in the ability to resolve tiny quantities of tracer nuclei with the general resolving power of MRI-techniques. On the other hand, the imaging dose (or acquisition time)

needed to record the signal of each voxel grows with the total number of pixels desired in the image, since the signal from the imaged voxel needs to be discernible in the strong background signal from the whole sample. This becomes problematic when this modality is to be used to image larger sample volumes with good resolution.

Future designs for gamma-MRI setups will certainly cover a larger solid angle of gamma-detectors around the sample, which would allow reaching a better signal to noise ratio in a shorter time. Further, the CMZ-pulse sequence and the connected image reconstruction method are, in comparison to the sequences used in modern MRI, rather straightforward. By learning from modern MRI algorithms (together with the group of Jean-Noël Hyacinthe), it seems very feasible that more efficient algorithms can be developed.

It should in general be possible to perform a gamma-MRI type measurement where the detectors are combined with collimators that limit the sample volume imaged at any one time. This would result in a SPECT-type image where each pixel of the SPECT image can be further resolved by the gamma-MRI method into a potentially large number of sub-pixels. However, the collimators would also absorb a significant portion of the gamma rays and thereby make the already long image-acquisition time ([1] reported over eight hours for their images) even longer, so progress on acquisition time should precede this step.

Another possible branch to take is to focus on different tracer isotopes, selected due to possibly even better asymmetry parameters of their gamma-emission and perhaps medically interesting behavior, such as increased concentration of the tracer in specific types of tissue. However, the change of isotope, especially when leaving the group of noble gases, would come with a number of new challenges. First and foremost, SEOP as a polarization scheme is only possible with noble gases. This can potentially be replaced by using Dynamic Nuclear Polarization (DNP)[1] or direct laser polarization. Further, other tracers may be administered in different ways than respiration, but the administration and distribution in the tissue must not exceed

[1] Which is also area of proficiency represented in the collaboration

the longitudinal relaxation time, lest the polarization is lost before the imaging can be performed. Further, it is desirable to use an isotope that directly decays to stable daughter nuclei, since a decay chain would mean an additional dose of administered radiation that can not be used for imaging. This argument makes isomeric states, such as those of ^{131m}Xe, so attractive for the method. Still, it might be worth researching if an efficient polarization scheme can be found for a nucleus whose daughter nucleus is ideal for imaging, since polarization is often maintained to a significant degree through the radioactive decay. The anisotropy tool (section 4.1) is also suitable to simulate the feasibility of such schemes.

Appendix A

Delay Study Reproduction

In order to confirm the correct functionality of the gamma-MRI simulation, the "CMZ delay study" presented in [13] was reproduced. Similar to the CMZ algorithm discussed in chapter 3, this study records the count-rate of the longitudinal detector before and after two consecutive RF pulses, which are separated by a delay time t_{delay}. Because the magnetization precesses in the transverse plane during the delay time, the azimuthal angle before the second RF-pulse depends on the t_{delay} and is converted into a polar angle by the second RF-pulse, resulting in a longitudinal count-rate that depends on t_{delay}. Figure A.1 shows the ratio of the longitudinal count-rate after and before the two pulses.

In order to achieve a direct comparison, all parameters were set according to the specifications made in [13]. The values are shown in table A.1. One might be

TABLE A.1: Parameters used to reproduce the CMZ delay study from [13].

Variable	**Value**	**Unit**	
`B_hold`	0.7	mT	specified
`Polarization`	0.57	-	specified
`RF_amplitude`	0.5	mT	estimated
`t_90`	0.363	ms	estimated

surprised by the fact that the sinusoidal result seen in figure A.1 does not start at a phase angle of zero. This is due to the fact that precession also occurs during the RF-pulses. Therefore, `RF_amplitude` and `t_90` determine the phase offset in the resulting plot and were estimated so that the simulation exhibits the same phase angle as the measurement.

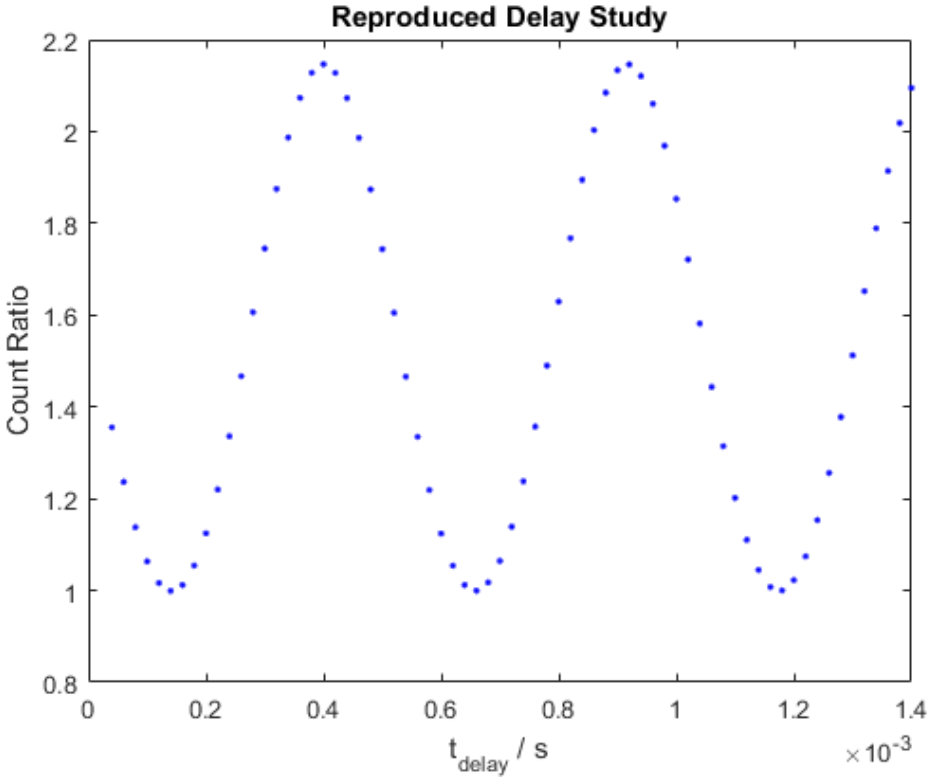

(A) Delay study reproduced by the simulation.

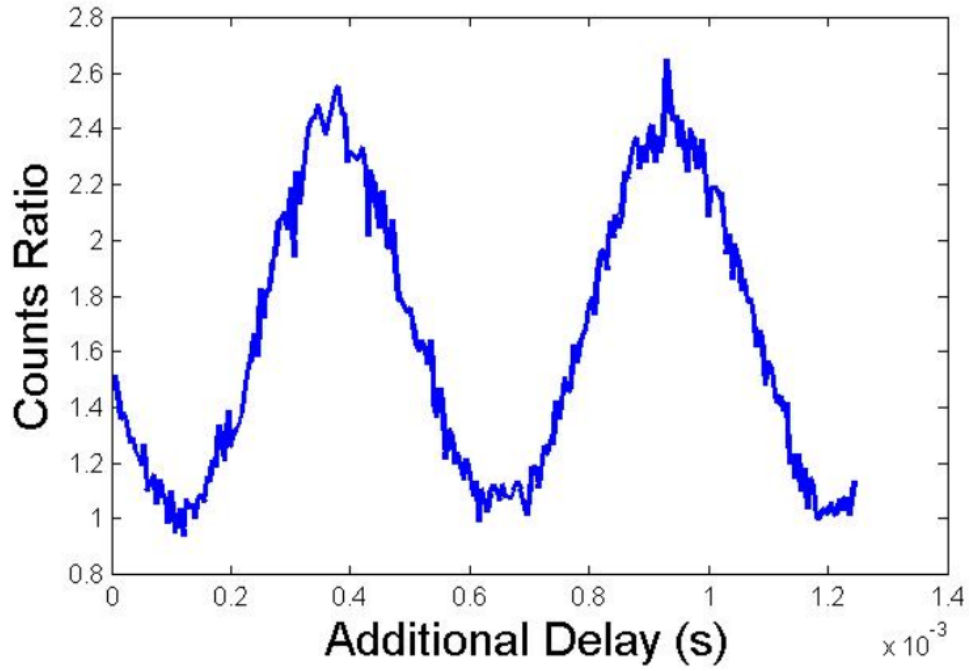

(B) Delay study measured and presented in [13].

FIGURE A.1: Comparison between the delay study published in [13] and its reproduction with the simulation code presented in this work.

Appendix B

Imaging Mathematics

$$2\pi\mathbf{k} = 2\gamma_{Xe}\tau\mathbf{G} \tag{B.1}$$

Angular Emission:

$$W(\theta) = \sum_{\lambda} A_\lambda B_\lambda P_\lambda(\theta) \tag{B.2}$$

$$= a_0 + a_2 cos(2\theta) + a_4 cos(4\theta) + ... \tag{B.3}$$

$$\simeq a_0 + a_2 cos(2\theta) \tag{B.4}$$

$$\tag{B.5}$$

Count-rate in any longitudinal detector.

$$S = C \int_V \rho(\mathbf{r}) W(\mathbf{k}, \mathbf{r}) d^3 r \tag{B.6}$$

Longitudinal count-rate contributions after CMZ sequence from one nucleus.

$$W_R(\mathbf{k}, \mathbf{r}) = a_0 - a_2 \cos(2\pi\mathbf{k} \cdot \mathbf{r}) \tag{B.7}$$

$$W_I(\mathbf{k}, \mathbf{r}) = a_0 + a_2 \sin(2\pi\mathbf{k} \cdot \mathbf{r})$$

Consider

$$
\begin{aligned}
S_c + iS_s &= C \int_{V_{Sam}} \rho(\mathbf{r}) W_R(\mathbf{k}, \mathbf{r}) d^3r \\
&+ C \int_{V_{Sam}} \rho(\mathbf{r}) W_I(\mathbf{k}, \mathbf{r}) d^3r \\
&= C \int_{V_{Sam}} \rho(\mathbf{r})[a_0 - a_2 \cos(2\pi \mathbf{k} \cdot \mathbf{r})] d^3r \\
&+ iC \int_{V_{Sam}} \rho(\mathbf{r})[a_0 + a_2 \sin(2\pi \mathbf{k} \cdot \mathbf{r})] d^3r \\
&= (1+i) a_0 C \int_{V_{Sam}} \rho(\mathbf{r}) d_3r \\
&+ a_2 C \int_{V_{Sam}} \rho(\mathbf{r}) - \cos(2\pi \mathbf{k} \cdot \mathbf{r}) + i \sin(2\pi \mathbf{k} \cdot \mathbf{r}) d_3r \\
&= (1+i) a_0 C \int_{V_{Sam}} \rho(\mathbf{r}) d_3r - a_2 C \int_{V_{Sam}} \rho(\mathbf{r}) e^{-i2\pi \mathbf{k} \cdot \mathbf{r}} d_3r \\
&:= A_0 - A(\mathbf{k})
\end{aligned}
$$

Resulting in the definitions:

$$A_0 = (1+i) a_0 C \int_{V_{Sam}} \rho(\mathbf{r}) d_3r \tag{B.8}$$

$$A(\mathbf{k}) = a_2 C \int_{V_{Sam}} \rho(\mathbf{r}) e^{-i2\pi \mathbf{k} \cdot \mathbf{r}} d_3r \tag{B.9}$$

Considering these, we find $A(\mathbf{k})$ and $\rho((r))$ to be a Fourier-pair with the FT definitions:

$$f(x) = \int_{-\infty}^{\infty} F(k) e^{2\pi i k x} dk \tag{B.10}$$

$$F(k) = \int_{-\infty}^{\infty} f(x) e^{-2\pi i k x} dx \tag{B.11}$$

We can reconstruct the image:

$$\rho(\mathbf{r}) = \frac{1}{a_2 C} \int_{V_k} A(\mathbf{k}) e^{2\pi i \mathbf{k} \cdot \mathbf{r}} d_3k \tag{B.12}$$

When comparing these calculations to the results published in [1], one might notice the opposite sign of the a_2-terms in equations B.7, whereas in previous publication from the same authors [13], the signs are the same as presented here. I therefore present the results that I retrieve from reproducing the derivations to my best understanding.

When reproducing the CMZ algorithm with the simulation code presented in chapter 4.2, it can be shown that the second RF-pulse, when starting with a phase angle of zero, turns the magnetization in the same direction as the first RF-pulse, resulting in an overall rotation of 180°. This is somewhat at odds with the description in [1], where a rotation of 90° and −90° seems to be described. Due to the 180°-symetry of the gamma-radiation, this is of little consequence for the overall method. Still, my simulations have shown that the negative sign of the second RF-pulse angle could be achieved by starting the second RF pulse with a phase angle of 180°. The effect would be a different rotation matrix 3.14 resulting in different signs in the equations B.7. While I have not found a direct mention of this in the publications, it is my best assumption that such a phase-shift of the second RF-pulse was used for the mathematics presented in [1].

Appendix C

gamma-MRI Simulation code

C.1 Script: Simulation

```
%% Simulation 2.0

clear
close all
global gamma


dt = 1e-7;
N = 400; % steps per sequence, used for preinitialization of variables
%t = dt:dt:N*dt;

T1 = inf;%20;
T2 = inf;%20e-5;

activity = 30e6;
voxdistance = 0.5;
plotscale = .1; % size of voxel representations in plot


%sample location
Sample_xlimits = [9,11];
Sample_ylimits = [9.5,9.5];
Sample_zlimits = [1, 1];

B_hold = 0.1; %T
%B_hold = 0.0007;
B_center = [(Sample_xlimits(1)+Sample_xlimits(2))/2,(Sample_ylimits(1)+
    Sample_ylimits(2))/2,(Sample_zlimits(1)+Sample_zlimits(2))/2]; %
    center of Bfcn, where Bfcn = B_hold
Bfcn = @(position, gradients) B_hold + (position-B_center)*gradients; %
     function handle used to calculate the local field


A = [-0.88902,0.44341]; % Transition coefficients A2 and A4 for -11/2
    to 3/2 M4
polarization = 0.57;
B = [1.1296,0.084389]*polarization; % Orientation parameters
```

```
34
35 %B(2) = 0; %removing fourth order for testing
36
37 % physical constants
38 hq = 1.051e-34; %Js
39 mu_n = 5.051e-27;%J/T
40 mu_Xe131m = -0.994*mu_n;
41 I = -11/2*hq;
42 gamma = mu_Xe131m/I; % [Hz/T]
43
44
45
46 %% Make Detectors
47
48 det_prob = 0.65; % detection probability of detector
49 sens_dist = 1; %distance between sensors within detector
50
51 figure(1)
52 hold on
53 %detector(xlimits, ylimits, zlimits, sensor_sidelength,
       detection_probability, ID)
54 xlimits1 = [-10];
55 ylimits1 = [10,10];
56 zlimits1 = [1 ,1];
57 det1 = detector(xlimits1,ylimits1,zlimits1, sens_dist, det_prob, 1, '
       red');
58 xlimits2 = [10,10];
59 ylimits2 = [10,10];
60 zlimits2 = [30];
61 det2 = detector(xlimits2,ylimits2,zlimits2, sens_dist, det_prob, 2, '
       blue');
62 xlimits3 = [30];
63 ylimits3 = [10, 10];
64 zlimits3 = [1,1];
65 det3 = detector(xlimits3,ylimits3,zlimits3, sens_dist, det_prob, 3, '
       green');
66
67 detectors = {det1,det2,det3};
68
69 xlim([-1,41])
70 ylim([-1,41])
71 zlim([-1,41])
72 xlabel('x / mm')
73 ylabel('y / mm')
74 zlabel('z / mm')
75 grid on
76 view(3)
77
78 %% Make Sample
79 % voxel(loc, theta_0, phi_0, A, B_factor, activity)
80
81 sample1 = sample(Sample_xlimits, Sample_ylimits, Sample_zlimits,
       voxdistance, A, B, activity, Bfcn, T1, T2, 1, true);
82
83 figure(1)
84 sample1 = sample1.make_hedgehogs(40);
85
86 sample1.voxels.sam_1_vox_0.activity = sample1.voxels.sam_1_vox_0.
       activity *0;
87 sample1.voxels.sam_1_vox_1.activity = sample1.voxels.sam_1_vox_1.
       activity *0;
```

```
88 sample1.voxels.sam_1_vox_2.activity = sample1.voxels.sam_1_vox_2.
       activity *0; % inserting some further inhomogenity to the "image"
89 % sample1.voxels.sam_1_vox_3.activity = sample1.voxels.sam_1_vox_3.
       activity *0;
90 % sample1.voxels.sam_1_vox_4.activity = sample1.voxels.sam_1_vox_4.
       activity *0;
91 % sample1.voxels.sam_1_vox_5.activity = sample1.voxels.sam_1_vox_5.
       activity *0;
92 % sample1.voxels.sam_1_vox_6.activity = sample1.voxels.sam_1_vox_6.
       activity *0;
93 %% Prepare Image
94 % This section computes an artificial perfect image and its fft for
       later comparison
95
96 p = 1;
97 for i = 1:1+floor((Sample_xlimits(2)-Sample_xlimits(1))/voxdistance)
98 for j = 1:1+floor((Sample_ylimits(2)-Sample_ylimits(1))/voxdistance)
99 Perfect_Image(i,j) = sample1.voxels.(sample1.voxnames{p}).activity;
100 p = p+1;
101 end
102 end
103 clear i j
104 figure(7)
105 imagesc(Perfect_Image)
106 Perfect_fft = fftshift(fft2(Perfect_Image))
107 Perfect_reconstr = ifft2(ifftshift(Perfect_fft))
108 imagesc(Perfect_reconstr)
109
110 %sample1 = sample1.yrot(pi/3); % rotation pre sequence
111
112 figure(1)
113 sample1 = sample1.plotme('hedgehog',plotscale);
114 pol = zeros(1,N);
115 hold on
116
117 %Pre-initializing rays
118 for d = 1:numel(detectors)
119 detectors{d} = detectors{d}.make_rays(sample1);
120 end
121
122 detcounts = zeros(3,N);
123
124 %% Measurement Sequence
125 % Skipped Improvements on RF-Pulses:
126 % Design a class RF-Pulse, with a method able to set the Bfcn of a
       sample in
127 % each dt-step according to an arbitrary RF-pulse-shape. Also implement
128 % off-resonance excitation via FT. (check necesssity/difference.)
129
130 %%% Delay Study
131 %         figure(1)
132 %
133 %         delay_times = [35*dt:2*dt:140*dt]; %mu seconds
134 %         delayed_answer = zeros(1, numel(delay_times));
135 %         RF_phase = 0;
136 %
137 %         for del = 1:numel(delay_times)
138 %             t_delay = delay_times(del);
139 %             [~, ~, CountBefore]  = sample1.evolve(20*dt,1, detectors,
       true, zeros(1,3));
140 %
```

```
%             [ReadCount, detectors,  phi, sample1] = CMZ(sample1, dt,
    t_delay,2*dt, detectors, B_hold, RF_phase, phi, [0;0;0]);
%
%             delayed_answer(del) = ReadCount(2)/CountBefore(2);
%             sample1 = sample1.repolarize([0,0,1],B);
%             figure(4)
%             plot(delay_times,delayed_answer,'b.')
%             xlabel('t_{delay} / s')
%             ylabel('Count Ratio')
%             title('Reproduced Delay Study')
%
%         end
%

%% run simple_precession
% N = 56; % timesteps
% [~, detectors, sample1] = simple_precession(sample1, dt, detectors,N
    /2 );
% sample1.voxels.sam_1_vox_0 = sample1.voxels.sam_1_vox_0.yrot(pi/2);
% [~, detectors, sample1] = simple_precession(sample1, dt, detectors,N
    );


%% CMZ Measurement
RF_phase = 0; % Initial phase angle of RF-pulses
RF_freq = abs( B_hold* gamma); %9.6856e5;
tau_larmor = 2*pi/(RF_freq);
Wr = zeros(sample1.Nxvox,sample1.Nyvox);
Ws = zeros(sample1.Nxvox,sample1.Nyvox);

%change these 2 if desired:
t_del = 1.1*tau_larmor;%  Delay time betwees rf pulses
t_grad = 1*tau_larmor; %   Time between pulses for which gradients are
    on.

t_del_r = t_del;
t_del_i = t_del + tau_larmor/8;
grad_strength = pi/(gamma * t_grad * voxdistance);

%selection of gradient values. Incorrect?
phi = [-sample1.Nxvox+1:1:sample1.Nxvox-1]*pi;
allgradients = phi./(voxdistance*(sample1.Nxvox-1)*gamma*t_grad)
for nx = 1:2*sample1.Nxvox-3
for ny = 1:sample1.Nyvox

gradients = [allgradients(nx);0;0]

%Real part
sample1 = sample1.repolarize([0,0,1],B); % resetting sample
[ReadCount, detectors,  phi, sample1] = CMZ(sample1, dt,t_del_r, t_grad
    , detectors, B_hold, RF_phase,  phi, gradients);
Wr(nx,ny) = ReadCount(2); %detector 2 count

%keyboard

%Imaginary part
sample1 = sample1.repolarize([0,0,1],B); % resetting sample
[ReadCount, detectors,  phi, sample1] = CMZ(sample1, dt,t_del_i, t_grad
    , detectors, B_hold, RF_phase,  phi, gradients);
Ws(nx,ny) = ReadCount(2); %detector 2 count
W_comp = Wr+i*Ws %intermediate display
```

```
196
197
198 end
199 end
200
201 W_comp = Wr+i*Ws;
202 W_corr = W_comp - mean(mean(W_comp)); %Substracting Offset
203 %F = fftshift(W_corr) % Center FFT % necessary?
204 F = ifft2(W_comp,'symmetric')
205 F = F/sum(sum(F))
206
207 figure()
208 imagesc(F)
209 title('recorded image')
210
211 figure()
212 Perfect_Image = Perfect_Image ./sum(sum(Perfect_Image)) % normalizing
    for comparison
213 imagesc(Perfect_Image)
214 title('ideal image')
215
216
217 %% Final Plotting
218 t = (1:numel(detectors{1}.count_history))*1e6; % time axis in
    microseconds
219 figure(2)
220 hold off
221 plot(t,detectors{1}.count_history,'Color', 'red')
222 hold on
223 plot(t,detectors{2}.count_history,'Color', 'blue')
224 plot(t,detectors{3}.count_history,'g-')
225 xlabel('time / microseconds')
226 ylabel('Counts per second')
227
228 legend('Transverse Det. 1','Longitudinal Det.','Transverse Det 2')
229 figure(1)
230 sample1 = sample1.plotme('hedgehog',sample1.voxdistance/2);
231 zlim([sample1.zlimits(1)-1, sample1.zlimits(2)+1])
232 ylim([sample1.ylimits(1)-1, sample1.ylimits(2)+1])
233 xlim([sample1.xlimits(1)-1, sample1.xlimits(2)+1])
```

C.2 Function: CMZ sequence

Called in the Simulation script:

```
1 function [ReadCount, detectors, phi, sample1] = CMZ(sample1, dt,
    t_delay, t_grad, detectors, B_hold, RF_phase, phi, gradients)
2 %% CMZ Imaging sequence
3 global gamma
4 RF_ampl = 5e-2; %T
5 RF_freq = abs( B_hold* gamma); %9.6856e5;
6 tau_larmor = 2*pi/(RF_freq);
7 t_90 = 3.63e-6;% dt*1.99;
8 t_readout = 10*dt;
9
10
```

```
if t_grad+dt > t_delay
error('Gradient time must not be greater than delay time.')
end

ReadCount = zeros(1,3);

% readout = false;
disp('Starting CMZ Sequence...')
j = 0;
state = 'starting';

while true
plothere = false;
j= j+1;
%Evolution
if j*dt<=t_90 %first RF pulse
state = 'Pulse 1 Running';
if j==1
disp('Starting Pulse Sequence. Starting RF Pulse 1...')
end
elseif (j-1)*dt <= t_90 && strcmp(state,'Pulse 1 Running')    %Activate
    gradients at the end of first RF pulse (called only once)
state = 'Ending Pulse 1, activating Gradients';
disp('... Delay time starting. Gradients on...')
plothere = false;

elseif j*dt<=t_90+t_grad && (strcmp(state,'Ending Pulse 1, activating
    Gradients')||strcmp(state,'Gradients active') )     %Precession (
    delay time ticking)
state = 'Gradients active';

elseif (j-1)*dt<=t_90+t_grad&& (strcmp(state,'Gradients active')) %
    Terminate gradients
state = 'Deactivating Gradients';
disp('...Deactivating Gradients...')
plothere = false;

elseif j*dt<=t_90+t_delay && (strcmp(state,'Deactivating Gradients')||
    strcmp(state,'Delay time active')) % Run Delay time
state = 'Delay time active';

elseif j*dt<=t_delay+2*t_90 && (strcmp(state,'Delay time active')||
    strcmp(state,'Pulse 2 Running')) %second RF pulse
if strcmp(state, 'Delay time active')
disp('...Ending delay time, Starting Pulse 2...')
plothere = false;
end
state = 'Pulse 2 Running';

elseif j*dt<= t_delay+2*t_90+t_readout && (strcmp(state,'Pulse 2
    Running')||strcmp(state,'Readout Time')) %Readout
if strcmp(state,'Pulse 2 Running')
disp('...Readout Time initiating...')
plothere = true;
end
state = 'Readout Time';

elseif j*dt>= t_delay+2*t_90+t_readout && strcmp(state,'Readout Time')
    % End
state = 'Sequence Complete';
disp('Sequence complete.')
```

```
else
warning('Inconsistency in the sequence! State: %s', state)
keyboard
end

switch state
case 'Pulse 1 Running'        %first RF pulse
RF_running = true;
[sample1, detectors] = sample1.evolve(dt,1, detectors, false, ReadCount
    , RF_ampl, RF_freq, RF_phase, j*dt);
%[sample1] = sample1.yrot(pi/2);

case 'Ending Pulse 1, activating Gradients' %Activate gradients at the
     end of first RF pulse (called only once)
sample1 = sample1.update_B(gradients);
RF_running = false;
[sample1]  = sample1.evolve(dt,1, detectors);

case {'Gradients active', 'Delay time active'} %Precession (delay time
     ticking)
[sample1, detectors]  = sample1.evolve(dt,1, detectors);

case 'Deactivating Gradients' %Deactivate Gradients (called only once)
sample1 = sample1.update_B([0;0;0]);
[sample1]  = sample1.evolve(dt,1, detectors);

case 'Pulse 2 Running' %second RF pulse
if ~RF_running % to remember begnning of pulse time
second_pulse_start = j;
end
[sample1, detectors]  = sample1.evolve(dt, 1, detectors, false,
    ReadCount, RF_ampl, RF_freq, RF_phase+pi, (j-second_pulse_start)*dt)
    ;
RF_running = true;
%[sample1] = sample1.yrot(pi/2);

case 'Readout Time' %Readout
RF_running = false;
[sample1, detectors, ReadCount]  = sample1.evolve(dt,1, detectors, true
    , ReadCount);

case 'Sequence Complete'
disp('...CMZ sequence complete.')
detectors{1} = detectors{1}.reset_count_history();
detectors{2} = detectors{2}.reset_count_history();
detectors{3} = detectors{3}.reset_count_history();
%          keyboard
break

otherwise
warning('Unassigned case occured: %s', state)
end


%Plotting
if plothere%
figure(1)
sample1 = sample1.plotme('hedgehog',sample1.voxdistance/2);
zlim([sample1.zlimits(1)-1, sample1.zlimits(2)+1])
ylim([sample1.ylimits(1)-1, sample1.ylimits(2)+1])
xlim([sample1.xlimits(1)-1, sample1.xlimits(2)+1])
```

```
119 end
120 clear m
121 pause(0.01)
122 if mod(j,35)==1 % plot every five steps
123 F2 = figure(2);
124 hold off
125 plot(detectors{1}.count_history,'Color', 'red')
126 hold on
127 plot(detectors{2}.count_history,'Color', 'blue')
128 plot(detectors{3}.count_history,'g-')
129 title('Detector Countrates')
130 end
131 %     phi(1,j) = vector_angle([0,0,1],sample1.voxels.sam_1_vox_0.M)/(pi
        );
132 %     %phi(2,j) = vector_angle([0,0,1],sample1.voxels.sam_1_vox_1.M)/(
        pi);
133 %     phi(3,j) = vector_angle([0,0,1],sample1.voxels.sam_1_vox_2.M)/(pi
        );
134 %     %phi(4,j) = vector_angle([0,0,1],sample1.voxels.sam_1_vox_3.M)/(
        pi);
135 %     phi(5,j) = vector_angle([0,0,1],sample1.voxels.sam_1_vox_4.M)/(pi
        );
136 %     %phi(6,j) = vector_angle([0,0,1],sample1.voxels.sam_1_vox_5.M)/(
        pi);
137 %     %phi(7,j) = vector_angle([0,0,1],sample1.voxels.sam_1_vox_6.M)/(
        pi);
138 %     %phi(8,j) = vector_angle([0,0,1],sample1.voxels.sam_1_vox_7.M)/(
        pi);
139 %
140 %     figure(3)
141 %     hold off
142 %     phi(phi==0)=NaN;
143 %     plot([1:length(phi)]*dt, phi)
144 %     title('Pixel angles to z axis')
145 %     ylabel('Azimuthal Angle / pi')
146 %
147 %     phi1(1,j) = vector_angle([0,1,0],sample1.voxels.sam_1_vox_0.M)/(
        pi);
148 %     phi1(2,j) = vector_angle([0,1,0],sample1.voxels.sam_1_vox_1.M)/(
        pi);
149 %     phi1(3,j) = vector_angle([0,1,0],sample1.voxels.sam_1_vox_2.M)/(
        pi);
150 %     phi1(4,j) = vector_angle([0,1,0],sample1.voxels.sam_1_vox_3.M)/(
        pi);
151 %     phi(5,j) = vector_angle([0,0,1],sample1.voxels.sam_1_vox_4.M)/(pi
        );
152 %     phi(6,j) = vector_angle([0,0,1],sample1.voxels.sam_1_vox_5.M)/(pi
        );
153 %     phi(7,j) = vector_angle([0,0,1],sample1.voxels.sam_1_vox_6.M)/(pi
        );
154 %     phi(8,j) = vector_angle([0,0,1],sample1.voxels.sam_1_vox_7.M)/(pi
        );
155 %
156 %     figure(99)
157 %     hold off
158 %     phi1(phi1==0)=NaN;
159 %     plot([1:length(phi1)]*dt, phi1)
160 %     title('Pixel angles to y axis')
161 %     ylabel('Azimuthal Angle / pi')
162 end
```

Appendix D

Dose Planning and Risk Considerations for the Decay Setup

D.1 Possible Incidents

1. **Due to a fast gas flow, liquid iodine solution gets into the tubing.**
   Likelyhood: Likely
   Consequences: Light
   Some of the Iodine will be outside of the well-shielded container. Subsequent operation steps will come with a higher administered dose. If all the iodine gets into the tubing, the dose rate while operating the valve between the filter and the source container rises to $31\mu Sv/h$ to the torso (40cm). The Iodine should still be stopped in the filter. In case the filter fails, the collected Xenon will be unusable. A small amount of contaminated gas could get into the AtmosBag when the cold trap is disconnected.
   Noticeability: Difficult
   This error would likely remain unnoticed if the magnitude is small, unless radiation meters start measuring higher values.
   Preventory Measures:
   The Source container is designed with an angled exit-pipe, in order to allow liquid in the pipe to flow back into the reservoir.

2. **The AtmosBag is punctured**
   Likelyhood: unlikely
   Consequences: Light
   At no point should significant levels of contamination be present in the atmosbag. Small leakages will be vented out by the fume hood to a large extend.
   Noticeability: Easy
   Any larger holes will be noticed since the AtmosBag would deflate. Even smaller holes are likely to be noticed visually.
   Emergency Measures:
   A small or medium hole can be easily fixed using the sealing tape of the AtmosBag.

3. **The piping develops a gas-leak.**
   Likelyhood: Rather unlikely
   Consequences: Light
   Some oft he gas escapes into the AtmosBag. Depending on the location on the leak within the setup, this will mainly contain Xenon contamination.
   Noticeability: Difficult
   Would only be noticed if radiation inside the AtmosBag rises and this is displayed on one of the radiation meters.
   Likely Magnitude: Small
   Since the loop is operated lose to normal pressure, only a very large hole would result in a significant gas-exchange with the Nitrogen in the Atmosbag.
   Preventory Measures:
   The system will be tested for a vacuum-level seal immediately before operation.
   Emergency Measures:
   Empying the Atmosbag through the filter and closing all valves. This would isolate the leak from the source, unless it is within the source container. Then it must be decided if the leak can be fixed and the experiment continued, or the setup must cool down as it is.

4. **The AtmosBag is punctured at a time when the Nitrogen inside is contaminated due to another simultaneous incident.**
   Likelyhood: Very unlikely
   Consequences: Medium to Severe
   Depending on the hole size and contamination level, this can release significant amounts of contaminated air into the fume hood.
   Emergency Measures:
   Under most circumstances, it should be possible to fix the AtmosBag very quickly. Otherwise, the Experiment must be stopped, all valves closed, the fume hood closed and left to cool down until radiation levels allow further cleanup.

5. **The Source vial drops and breaks while being lifted from the packaging to the source container.**
   Likelyhood: Extremely unlikely
   Consequences: Severe
   The Iodine is spilled within the Atmosbag, which is not well suited to contain liquid iodine over long periods.
   Preventory Measures:
   - The procedure will be tested and trained with an empty vial in advance.
   - Suitable tongues will be used to hold the vial.
   - The vial will not be lifted more than 10cm over the surface.
   Emergency Measures:
   The Remainder of the vial and its containing iodine must be moved into one of the two available sealable containers and the container closed. The Atmosbag must now be continuously vented through the filter until radiation levels drop to a safe level for further cleanup. It might be necessary to put the fumehood and possibly the lab under a quarantine for a span of weeks until radiation has cooled down and the cleanup can be completed.

Bibliography

[1] Yuan Zheng, G Wilson Miller, William A Tobias, and Gordon D Cates. A method for imaging and spectroscopy using γ-rays and magnetic resonance. *Nature*, 537(7622):652, 2016.

[2] H. Postma N.J. Stone. *Low-Temperature Nuclear Orientation*. North-Holland Physics Publishing, 1986. ISBN 0-444-86994-8.

[3] Olaf Dössel. *Bildgebende Verfahren in der Medizin, Von der Technik zur Medizinischen Anwendung*. Springer Vieweg, 2 edition, 2016. ISBN 978-3-642-54406-4.

[4] Richard B. Firestone. Table of isotopes. cd rom edition. 1996. Version 1.0.

[5] Penelope Bouziotis and Carlo Fiorini. Spect/mri: dreams or reality? *Clinical and Translational Imaging*, 2(6):571–573, 2014.

[6] M Kowalska, P Aschenbrenner, M Baranowski, Mark L Bissell, W Gins, RD Harding, H Heylen, G Neyens, Stavroula Pallada, N Severijns, et al. New laser polarization line at the isolde facility. *Journal of Physics G: Nuclear and Particle Physics*, 44(8):084005, 2017.

[7] HA Tolhoek and JAM Cox. Angular distribution and polarization of gamma radiation emitted by oriented nuclei. *Physica*, 19(1-12):101–119, 1953.

[8] Grace MA Blin-Stoyle RJ. Oriented nuclei. In S Flügge, editor, *Encycopedia of Physics XLII: Nuclear Reactions III*, volume 42, page 555. Springer Verlag, 1957.

[9] Jack K. Becconsall Horst Friebolin. *Basic One- and Two-Dimensional NMR Spectroscopy*. WILEY-VCH, 3 edition, 1998. ISBN 3-527-29513-5.

[10] Jean-Noël Hyacinthe. *Développements méthodologiques en RMN du 129Xe hyperpolarisé en vue d'applications à la mesure de la perfusion cérébrale chez le petit animal*. PhD thesis, Université Joseph Fourier (Grenoble), 2004.

[11] W Happer, E Miron, S Schaefer, D Schreiber, WA Van Wijngaarden, and X Zeng. Polarization of the nuclear spins of noble-gas atoms by spin exchange with optically pumped alkali-metal atoms. *Physical Review A*, 29(6):3092, 1984.

[12] Thomas Meersmann and Eike Brunner. *Hyperpolarized xenon-129 magnetic resonance: concepts, production, techniques and applications*. Number 4. Royal Society of Chemistry, 2015.

[13] Yuan Zheng. *Low Field MRI and the Development of Polarized Nuclear Imaging (PNI) - A New Imaging Modality.* PhD thesis, University of Virginia, 9 2014.

[14] Daniel A Steck. Rubidium 87 d line data, 2001.

[15] Joseph S Six, Theodore Hughes-Riley, Karl F Stupic, Galina E Pavlovskaya, and Thomas Meersmann. Pathway to cryogen free production of hyperpolarized krypton-83 and xenon-129. *PLoS One*, 7(11):e49927, 2012.

[16] T Yamazaki. Tables of coefficients for angular distribution of gamma rays from aligned nuclei (nuclear data sheets, section a). *Nucl. Data, Sect. A, 3: No. 1, 1-24 (Aug. 1967).*, 3(UCRL–17086), 1967.

[17] James M Bright, Trenton T Rees, Louis E Baca, and Richard L Green. Volatility of radiopharmacy-prepared sodium iodide-131 capsules. *Journal of nuclear medicine technology*, 28(1):52–55, 2000.

[18] Ellsworth J Browning, Krishnadas Banerjee, and William E Reisinger Jr. Airborne concentration of i-131 in a nuclear medicine laboratory. *Journal of nuclear medicine: official publication, Society of Nuclear Medicine*, 19(9):1078–1081, 1978.

[19] Pin Jern Ker, John PR David, and Chee Hing Tan. Temperature dependence of gain and excess noise in inas electron avalanche photodiodes. *Optics express*, 20(28):29568–29576, 2012.

[20] Y Kamisho, M Mihara, K Matsuta, M Fukuda, M Yaguchi, M Wakabayashi, Y Morita, J Ohno, S Shinozaki, R Kambe, et al. Development of the pulse nmr method utilizing the short-lived β-emitter 12b. *Hyperfine Interactions*, 222 (1-3):121–125, 2013.

[21] R Engel. Preparation of transversal relaxation time measurements using beta-nmr at the vito beamline. Technical report, ISOLDE, CERN, 2018.

[22] M Kowalska. Collection of 133mxe for mri+spect feasibility study. Technical Report CERN-INTC-2017-092, CERN, 2017.

Contributions

The development of the gamma-MRI project at ISOLDE was presented in form of a Poster at the *ISOLDE Workshop and Users Meeting 2017* under the title *Exploring Gamma-Detected Magnetic Resonant Imaging* and in the medical physics section of the *DPG-Fruehjahrstagung 2018* in Würzburg as a talk of the title *Towards gamma-MRI: First Setup Performance.*

Declaration of Authorship

I hereby certify that this thesis has been composed by me and is based on my own work except where indicated otherwise. I have not used any references or verbatim extracts other than those quoted, and all sources of information, including graphs and data sets, have been specifically acknowledged. Additionally I certify that I followed the general principles of scientific work and publication, as they are specified in the guidelines for good scientific practice of Carl-von-Ossietzky Universität Oldenburg.

Date: Signed: